The Gulf Stream Extension Region: Its dynamics and interaction with the atmosphere

Diploma Thesis written by

Martin Claus
<mclaus@ifm-geomar.de>

Mathematisch - Naturwissenschaftliche Fakultät der
Christian-Albrechts-Universität zu Kiel
Erstellt am Leibniz - Institut für Meereswissenschaften
Forschungsbereich 1
- Theorie und Modelierung -

Kiel, October 11, 2011

Contents

Abstract

The Gulf Stream Extension Region is a key region for meridional heat transport of the Earth system. Its importance for the climate and for seasonal prediction has been increasingly recognized in recent years. However, the dynamics of the ocean in this region are not understood sufficiently. There are basically three mechanisms to explain the observed increase of barotropic transport and the formation of recirculation gyres in the Gulf Stream Extension Region: (i) advection of potential vorticity, (ii) Joint Effect of Baroclinicity and Relief and (iii) eddy momentum flux, of which the latter is investigated in the present work.

16 years of satellite derived surface velocities of weekly resolution are used to compute the eddy momentum flux and its seasonal and NAO related variability. These fluxes were used to drive a diagnostic linear shallow water model to estimate the mean barotropic transport and its variability associated with turbulent momentum flux. The results show that eddy momentum flux is able to drive significant transport in the Gulf Stream Extension Region, enough to explain its observed increase. The barotropic transport streamfunction exhibits northern and southern recirculation gyres between the separation point at Cape Hatteras and the Newfoundland Ridge and also resemble mesoscale circulation features like the Mann eddy. The seasonal transport variability is shown to be large upstream of the Grand Banks of Newfoundland with the strongest signal where the Gulf Stream crosses the New England Seamounts at about 62°W. The NAO appears to significantly affect the strength of the northern and southern recirculation gyres during the winter season leading to an increased mean transport in winters with a positive NAO index.

Acronyms

ADCP	Acoustic Doppler Current Profiler
AGCM	atmospheric general circulation model
AMOC	Atlantic Meridional Overturning Circulation
BC	boundary condition
CFL	Courant–Friedrichs–Lewy
DWBC	deep western boundary current
EKE	eddy kinetic energy
EMF	eddy momentum flux
ETOPO1	1 Arc-Minute Global Relief Model
FC	Florida Current
GS	Gulf Stream
GSER	Gulf Stream Extension Region
JEBAR	Joint Effect of Baroclinicity and Relief
NA	North Atlantic
NAC	North Atlantic Current
NAO	North Atlantic Oscillation
NES	New England Seamounts
NRG	northern recirculation gyre
OGCM	ocean general circulation model
PV	potential vorticity

SLP	sea level pressure
SST	sea surface temperature
SWM	Shallow Water Model

Chapter 1

Introduction

1.1 Importance of the Gulf Stream for northern hemisphere climate

The Gulf Stream (GS) consists of a wind driven component and the upper limb of the Atlantic Meridional Overturning Circulation (AMOC) (*Schmitz and Richardson*, 1991). Its importance for meridional heat transport and thereby northern hemisphere climate is well known (*Wunsch*, 2005; *Trenberth and Caron*, 2001; *Seager et al.*, 2002). In the Gulf Stream Extension Region (GSER) large amounts of latent and sensible heat are released to the atmosphere, especially in winter time (annual mean: $\sim 200\,\mathrm{W\,m^{-2}}$ latent heat flux, $\sim 50\,\mathrm{W\,m^{-2}}$ sensible heat flux; *Yu and Weller*, 2007). Winter time diabatic heating of the atmosphere in the GSER causes strong onshore temperature gradients, which creates a highly baroclinicly unstable environment. Observations indicate that the degree of low-level baroclinicity significantly affects the rate of deepening of cyclones in this region (*Cione et al.*, 1993). Furthermore the path of these storms is anchored over the GS sea surface temperature (SST) front and reaches out as far as northern Europe (*Hoskins and Hodges*, 2002). These influences on synoptic scales extend onward to longer time scales and might have an effect on the atmospheric general circulation, as argued by *Minobe et al.* (2008).

Ocean currents are mainly driven by wind stress and surface buoyancy fluxes determined by the atmosphere. These currents provide important contributions to the local heat budget and therefore influence the thermodynamics of the overlying atmosphere. *Bjerknes* (1964) identified two kinds of atmosphere-ocean interactions: the first one is the quasi-instantaneous response of SST to surface air temperature and wind due to latent and sensible heat flux (*Cayan*, 1992). The second one is the change of ocean circulation due to variation in surface wind stress or meridional overturning and therefore alteration in ocean heat transport convergence and SST, which is of more sluggish nature. In the North Atlantic (NA), the dominant mode of

atmospheric variability is the North Atlantic Oscillation (NAO), which has a robust spatial pattern of air-sea interaction but is largely stochastic in time due to synoptic excitation. Experiments with simple stochastic models reveal that thermal coupling of the atmosphere and ocean reddens both of their spectra (*Barsugli and Battisti*, 1998). On time scales long enough for advection to play a role, the response of NA SST shows a preferred time scale of the order of a decade (*Saravanan and McWilliams*, 1998). *Marshall et al.* (2001) included both gyre circulation and AMOC in their model and proposed, that each of them lead to a delayed oscillator effect, which can act to offset the strong local damping of SST. This is in general agreement with a more complex experiment of *Eden and Greatbatch* (2003). They found two acting feedbacks on the NAO: a fast positive feedback due to surface heat fluxes as well as barotropic adjustment of the ocean to wind stress changes and a slow negative feedback due to changes in the AMOC.

1.2 Dynamics of the Gulf Stream

The systematic survey of the ocean circulation in the NA began in the 1920s and 30s with a series of hydrographic station measurements (e.g. *Wüst*, 1935). One of the famous results of these early campaigns is the 10 °C isotherm map published by *Iselin* (1936) and shown as Figure 1.1, clearly showing the large-scale average features of the NA circulation. The GS appears as a narrow and swift stream band, detaching from the shelf break at Cape Hatteras (35.5°N 75.5°W), crossing the Hatteras Abyssal Plain, the New England Seamounts (NES) Chain and the Sohm Abyssal Plain to reattach again at the southern tip of the Grand Banks of Newfoundland and the Newfoundland Ridge (see Figure 1.2). The sharpness of the current and the striking cross-basin asymmetry of the gyre inspired *Stommel* (1948) to his theory of western intensification of wind-driven ocean currents. He identified the latitudinal variation of the Coriolis parameter to be the reason for the formation of western boundary currents.

Ongoing technical development increased the resolution and precision, which gave a chance to map the synoptic GS front associated with the Stream axis. The multi-ship mission "Operation Cabot", launched in June 1950, finally succeeded in revealing the meandering structure of the Stream and documented the formation of a cold core ring, pinching off into the Sargasso Sea (*Fuglister and Worthington*, 1951). But the energy source of the meanders remained unclear. *Webster* (1961) estimated the direction of eddy momentum flux (EMF) from surface velocity in the Florida Current (FC) and surprisingly found a flux of momentum into the jet, suggesting that kinetic energy of the mean flow is not the source of energy for meanders. In his classical paper, *Thompson* (1971) argued that topographic Rossby waves, having a group velocity pointing away from the jet, will transport momen-

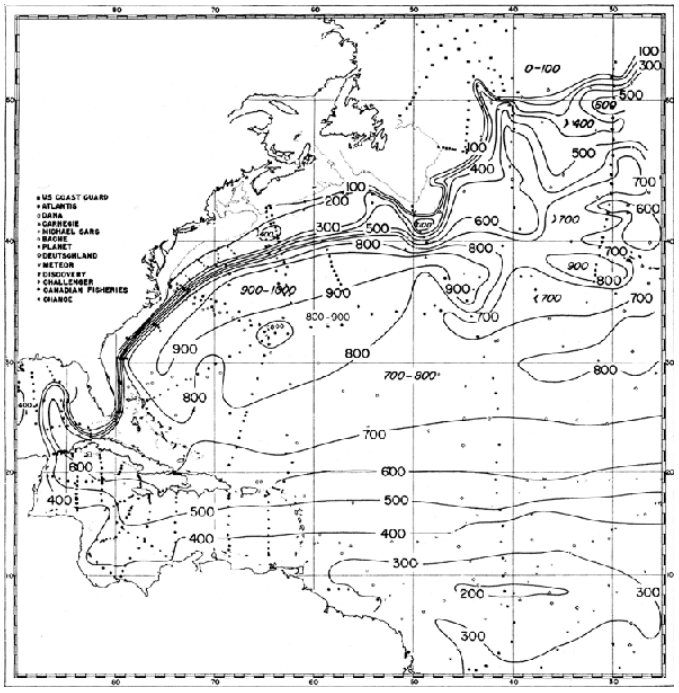

Figure 1.1: *Chart of the depth of the* 10 °C *Isotherm in the western NA (after Iselin, 1936).*

tum in the opposite direction. Finally, based on observed growth rates and wavelengths, *Hansen* (1970) proposed baroclinic instability as the relevant process for the evolution and growth of meanders, hence available potential energy as their energetic source.

The possibility of extending the hydrographic sections all the way down to the ocean floor revealed the equivalent barotropic structure of the GS (*Worthington*, 1954). Deployment of Swallow floats provided velocities of the deep current, which were used to reference the baroclinic velocity obtained by these sections. This made first estimates of volume transport available (*Fuglister*, 1963), revealing a huge increase in volume transport up to 147 Sv, which is five times more than the expected wind driven transport of 30 Sv based on flat-bottomed Sverdrup theory. The development and deployment of moored current meters allowed long term measurements and helped to draw a reliable map of mean depth integrated transport, leading to the discovery of the Worthington gyre (*Worthington*, 1976) and the Northern Recirculation gyre (*Hogg et al.*, 1986). These gyres, located south and north of the mean current, recirculate the water masses and therefore dramatically enhance the transport along the main stream.

Recirculation is not a feature of Stommel's simple linear flat-bottom model. It was *Fofonoff* (1954) who emphasized the importance of advection and therefore memory of the water parcel of its potential vorticity (PV).

Figure 1.2: *The GSER with bathimetry and schematic mean current (white arrows). At the Newfoundland ridge and downstream of it the northward flowing NAC successively turns to the east until it reaches the northwest corner where it makes a sharp turn to flow through the Charlie-Gibbs Fracture Zone.*

Veronis (1966) was the first to find numerical solutions to the non-linear version of Stommel's barotropic problem for a range of parameters from slightly to highly non-linear cases. The effect of non-linearity allows the western boundary current to penetrate into regions where there is no wind stress and the centre of the gyre is located more northward with increasing Rossby number (*Böning*, 1986). With the importance of advection and mixing of PV being increasingly recognised from observations (*Keffer*, 1985), *Marshall and Nurser* (1986) and *Greatbatch* (1987) extended Fofonoff's barotropic solution to a baroclinic ocean. The latter stated that northward advection of low PV by the western boundary current stretches downward the circulation until it intersects with the ocean floor. This, in turn, requires the presence of enhanced barotropic recirculation driven by eddies and dissipated by bottom friction. A different explanation of recirculation was raised by *Holland* (1973). He suggested bottom topography to be an important factor and introduced the bottom pressure torque to the linear vorticity equation. Diagnostic calculations of the NA basin revealed that this term is capable of producing recirculation gyres without the consideration of non-linear effects in the vorticity balance (*Mellor et al.*, 1982; *Greatbatch et al.*, 1991).

An alternative theory of recirculation was proposed by *Greatbatch et al.* (2010a), suggesting that mesoscale eddies, fed by baroclinic and barotropic instability, systematically flux easterly momentum into the core of the jet and drive the recirculation gyres in a zonally integrated sense. Mesoscale eddies are a prominent feature of many regions of the global ocean, especially the western boundary currents and the Southern Ocean (*Stammer and Wunsch*, 1999). Yet, their contribution to the mean circulation remains poorly understood, although they are assumed to be important (*Holland and Rhines*, 1980). In the atmosphere the interaction of eddies and mean flow is well known (*Marshall and Plumb*, 2008; *Wardle and Marshall*, 2000). In the ocean, however, the rough and steep bottom topography scrambles this picture and makes it difficult to see the local effect of eddy forcing. *Greatbatch et al.* (2010a) used the zonally integrated zonal momentum equation to simplify the analysis and indeed showed that the forcing by the eddies accelerate the zonal mean flow with a magnitude comparable to wind stress.

The goal of this thesis is to answer the question of how much transport can be driven by EMF and how much transport variability can be attributed to variability of the EMF. Chapter 2 presents a selection of Reynolds stress terms (synonymous with EMF) computed from satellite altimeter data: the long time mean, seasonal means and interannual variability associated with the NAO. In Chapter 3 a numerical model is formulated which is used to compute the barotropic transport driven by the EMFs. The result of these experiments are shown and discussed in Chapter 4. The results of the mean state experiment presented in Section 4.1 are basically the same as in *Greatbatch et al.* (2010b) since the very same model and forcing was used, but instead of linear friction, as in this thesis, a quadratic formulation was used

in the published paper. The impact of temporal variations of the EMFs on the barotropic transport are presented in Section 4.2 and 4.3, which shows a quasi-instantaneous response of transport to variations of the NAO. Finally, in Chapter 5 all results are summarised and discussed.

Chapter 2

Reynolds Stress

The Reynolds stress is the Eulerian average stress acting on a fluid due to turbulent fluctuations of motion. It is obtained by taking the variance and covariance of the velocity components over a period that is long enough for these fluctuations to be averaged out, i.e,

$$R_{ij} = \rho \, \overline{u_i' u_j'} \,, \tag{2.1}$$

where ρ is the fluid density and primes denote the anomaly with respect to a time-average. On large scales, the spatial fluctuations of density in the ocean are much smaller than that of velocity and can safely be neglected. Hence, the associated momentum flux in the momentum equation is

$$F_i = \rho \frac{\partial \, \overline{u_i' u_j'}}{\partial x_j} \,. \tag{2.2}$$

In the atmosphere meso-scale turbulence, i.e. baroclinic eddies, are the most important component of the mid-latitude general circulation (*Jeffreys*, 1926; *Starr*, 1948; *Lorenz*, 1967). The question of how these turbulent fluctuations can drive the zonal mean flow is well understood (*Kuo*, 1951; *Dickinson*, 1969; *Wardle and Marshall*, 2000). The eddies are distorted by the mean flow to their well known "banana-shape", which leads to convergence of the turbulent zonal momentum flux at the location of the zonal mean jet (*Marshall and Plumb*, 2008), as shown schematically in Figure 2.1.

In the ocean, however, the picture is not as clear although satellite observations provide data of global coverage and increasingly high temporal and spatial resolution. Some work has been done to estimate the effect of the EMF on the mean flow and it seems that the underlying bottom topography influences both the mean flow and Reynolds stresses (see *Ducet and Le Traon*, 2001; *Greatbatch et al.*, 2010a) and that the latter can locally either accelerate or decelerate the mean flow (*Hughes and Ash*, 2001). It is very likely that this complex relation emerges from the topographic distortion of

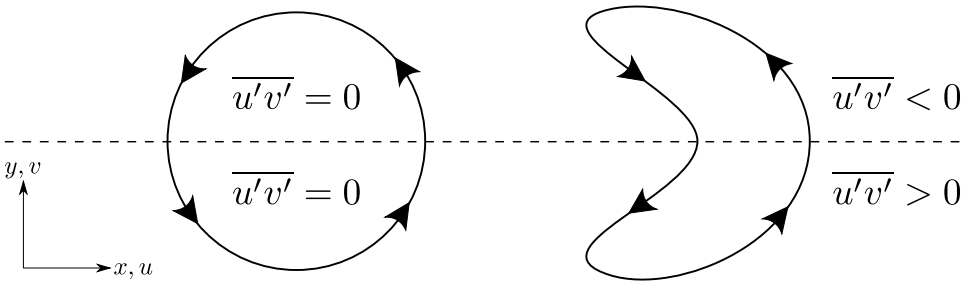

Figure 2.1: *The circular eddy (left) can not lead to EMF convergence at the axis of the jet in a zonally integrated sense. The banana-shaped eddy does show EMF convergence due to its distortion from a perfect circular shape by the mean jet. This is a reproduction of Figure 8.14 in Marshall and Plumb (2008)*

the eddies (*Greatbatch et al.*, 2010a) and thus no general conclusion can be drawn of how the EMF and mean flow interact.

In the GSER, *Greatbatch et al.* (2010a) showed that the Reynolds stress patterns are quite robust, perhaps because of the influence of the underlying topography. By zonally averaging the zonal momentum equation, the authors reduced the analysis of zonal momentum flux to the meridional gradient of zonally averaged Reynolds stress cross-covariance, i.e. $\overline{u'v'}$. This revealed that the most prominent features of the Reynolds stress cross-covariance, a dipole of positive values at Cape Hatteras and negative values at the Grand Banks of Newfoundland, are responsible for systematically fluxing westerly momentum into the zonally-averaged GS extension. This dipole is locked in place, where the GS separates from the continental slope and reattaches back again. Both poles are associated with along-slope flow variations, which are the preferred type of variations in these regions (*Scott et al.*, 2008). Further, *Greatbatch et al.* estimated the vertically and zonally integrated flux of zonal momentum and found its magnitude to be comparable to the input of momentum by wind stress. Indeed, this supports the hypothesis that the EMFs are capable of driving significant transport and locally break the directly wind-driven Sverdrup balance and hence drive the recirculation gyres. Since both poles are remotely connected by $\frac{f}{H}$ contour lines, they are able to form a closed loop and drive circulation similar to the northern recirculation gyre.

When considering temporal variability, the Reynolds stress patterns are even more difficult to interpret. The GS is subject to various kinds of variability, such as path shifts (*Lee and Cornillon*, 1995) or transport changes (*Kelly and Gille*, 1990; *Sato and Rossby*, 1995; *Rossby et al.*, 2010). These are, in turn, related to various factors such as variability of the deep western boundary current (DWBC) (*Joyce et al.*, 2000; *Zhang and Vallis*, 2007; *Peña Molino and Joyce*, 2008; *Joyce and Zhang*, 2010) or the atmospheric forcing (*Eden and Willebrand*, 2001; *Frankignoul et al.*, 2001; *de Coëtlogon et al.*, 2006) and can be found on seasonal to decadal time scales. *Zhai*

et al. (2008) found a distinct seasonal cycle of eddy kinetic energy (EKE) with relatively high values in summer and low values in winter. This is in contrast to production of EKE in terms of eddy growth rate, which is highest in late winter. The authors suggested that thermal capping in summer shields the eddies from thermal interaction with the atmosphere and that reduced wind speeds in summer reduce the mechanical damping, hence a lower dissipation rate is expected. This encourages investigation of the seasonal variation in barotropic transport associated with the seasonal variability of the EMF. Since mechanical damping of eddies is related to surface wind speed (*Duhaut and Straub*, 2006; *Zhai and Greatbatch*, 2007) in winter time, a quasi-instantaneous relation of Reynolds stress to the winter time NAO might be expected and will be investigated.

The main objective of this chapter is to supply the Reynolds stress terms, which are used to drive the model presented in Chapter 3. How these terms influence the mean flow is discussed in Chapter 4.

2.1 Data and Methods

To compute the EMFs, the geostrophic velocity, u and v, of a 16 year period from December 1994 to December 2010 are used. These velocities are obtained from the Delayed Time Ssalto/Duacs Gridded Absolute Geostrophic Velocities data set[1], which is compiled from merged along-track altimeter measurements of several satellite missions (Topex/Poseidon, Jason-1, Jason-2, GFO, ERS-1, ERS-2 and Envisat). This data set has a temporal resolution of a week on a 1/3° Mercator grid. The reader is referred to *Le Traon et al.* (1998) for further details about the dataset. The geostrophic velocity anomalies are computed by subtracting the time-average of the whole time series. The mean state Reynolds stress is obtained by time-averaging each of the terms $u'u'$, $v'v'$ and $u'v'$ over the complete 16 year period. By time-averaging only over the corresponding seasons (i.e. DJF, MAM, JJA and SON) and subtracting the annual mean Reynolds stress, the seasonal anomalous Reynolds stress is computed. The winter time variability of the Reynolds stress terms associated with the NAO is derived by binning the DJF data to their corresponding NAO phase and then taking the mean of each bin. Whether the phase is positive (negative) is decided using the DJF NAO-index of *Hurrell* (1995) defined as the normalized principal component time series of the leading EOF of DJF sea level pressure (SLP) over the Euro-Atlantic sector (20°N-80°N,90°W-40°E), available since 1899. If the index is above (below) its median of the period from December 1994 to February 2009 the phase is assumed to be positive (negative). This guarantees that both bins have approximately the same number of samples.

[1]The altimeter products were produced by Ssalto/Duacs and distributed by Aviso, with support from Cnes (http://www.aviso.oceanobs.com/duacs/). Compiled at 2011/03/29.

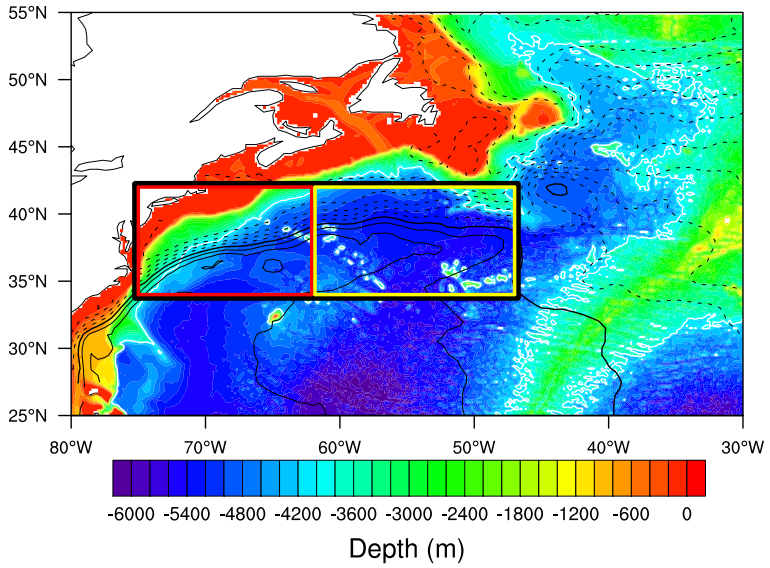

Figure 2.2: *Bathymetry of the GSER as shading and areas used in this chapter to compute area-weighted averages and variances. The* 4000 m *isobath is drawn as a white line and the mean dynamic ocean topography (Niiler et al., 2003) is contoured in black with an interval of* 10 cm*. It can be seen quite well how the GS follows the isobaths upstream of Cape Hatteras and downstream of the Newfoundland Ridge. The boxes are defined as follows: red* 34°N-42°N, 75°W-62°W *(referred to as UP); yellow* 34°N-42°N, 62°W-47°W *(referred to as DOWN); black is the union of red and yellow.*

While computing means, variances and pattern correlations for the analysis of the Reynolds stress, area weighting is applied throughout.

2.2 Results

2.2.1 Long-term mean

Figure 2.3 shows the spatial distribution of the Reynolds stress terms ($\overline{u'u'}$, $\overline{v'v'}$ and $\overline{u'v'}$) over the complete 16 year period and contours of the mean dynamic ocean topography, taken from *Niiler et al.* (2003), to indicate the mean flow by geostrophy. At first glance, high absolute values of all three Reynolds stress terms are confined to the main axis of the GS. The region of both zonal and meridional velocity variance ($\overline{u'u'}$ and $\overline{v'v'}$) higher than $0.14\,\mathrm{m^2\,s^{-2}}$ forms a narrow zonal band that extends from 37°N to 39°N and 73°W to 47°W (regions of green to red colour in Figure 2.3). Both reach their maximum with values of $0.36\,\mathrm{m^2\,s^{-2}}$ ($\overline{u'u'}$) and $0.29\,\mathrm{m^2\,s^{-2}}$ ($\overline{v'v'}$) where the GS crosses the NES (at 38.5°N, 62°W).

The velocity covariance ($\overline{u'v'}$, Figure 2.3(c)) reveals a different picture. Indeed values of high absolute covariance are again confined to the mean axis

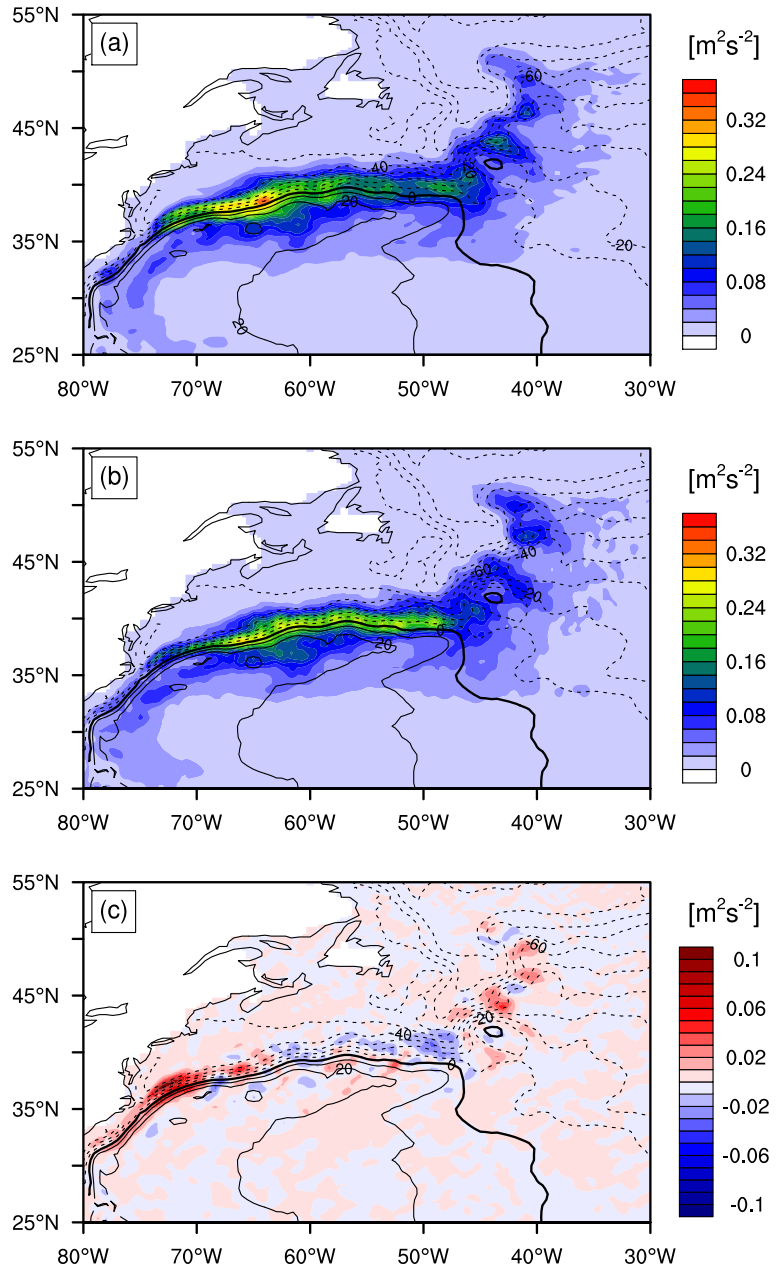

Figure 2.3: *Surface Reynolds stress terms averaged over the complete 16 year time series, with (a)* $\overline{u'u'}$*, (b)* $\overline{v'v'}$ *and (c)* $\overline{u'v'}$*. Contours of the mean dynamic ocean topography (Niiler et al., 2003) are drawn with an interval of* 10 cm *to indicate the mean path of the GS as areas of high gradient. Clearly, high values of Reynolds stress are located within the currents mean path. But in contrast to* $\overline{u'u'}$ *and* $\overline{v'v'}$*,* $\overline{u'v'}$ *exhibits a pronounced along-stream variation with a positive peak at Cape Hatteras (up to* $0.12\,\mathrm{m^2\,s^{-2}}$*, known as the "double blade" (Ducet and Le Traon, 2001)) and a negative peak at the south-east tip of the Newfoundland Ridge (*$-0.03\,\mathrm{m^2\,s^{-2}}$*).*

of the GS but in this case along-stream dipoles are the dominant structure. The largest dipole consists of an area of mostly positive values upstream the NES (75°W to 62°W) with its maximum of $0.12\,\mathrm{m^2\,s^{-2}}$ near Cape Hatteras, known as the "double blade" (*Ducet and Le Traon*, 2001), and an area of mostly negative values extending from 62°W to 47°W. The minimum is located at 49°W, where the GS reattaches to the continental slope and turns northward, having a value of $-0.03\,\mathrm{m^2\,s^{-2}}$. It is this zonally tilted dipole which is associated with the zonal momentum flux into the jet, at least in a zonally integrated sense (*Greatbatch et al.*, 2010a). Downstream of the Newfoundland Ridge following the northward heading branch of the stream, there are alternating patches of positive and negative velocity covariance. However, it is hard to see a local systematic flux of zonal momentum, which would have negative (positive) values of $\overline{u'v'}$ north (south) of the mean current axis. The patterns of Reynolds stress terms shown in Figure 2.3 are virtually identical to the results of *Ducet and Le Traon* (2001) and *Greatbatch et al.* (2010a), although the time period of data used in these papers (5.5 and 13 years) differs from the one in this thesis (16 years). Since all three distributions are rather robust in time, this is likely to reflect the influence of rough and steep bottom topography on mesoscale flow variability. This is even more supported by the fact that both the "double blade" and the minimum of $\overline{u'v'}$ at the Grand Banks are associated with flow variability along isobaths, which are shown in Figure 2.2.

2.2.2 Seasonal Variability

The seasonal anomalous Reynolds stress terms in the GSER are shown in Figure 2.4 for each individual season and their statistics are listed in Table 2.1 averaged over the region 34°N to 42°N and 75°W to 45°W (black box drawn in Figure 2.2). The velocity variances ($\overline{u'u'}$ and $\overline{v'v'}$) exhibit a distinct seasonal variability in the region 32°N to 42°N and 74°W to 45°W with an minimum in winter and a maximum in summer, consistent with the results of *Zhai et al.* (2008) and *Ducet and Le Traon* (2001) concerning the seasonal cycle of EKE. The range of area averages, listed in Table 2.1, of about $2.02 \cdot 10^{-2}\,\mathrm{m^2\,s^{-2}}$ for $\overline{u'u'}$ is slightly larger than that for $\overline{v'v'}$ ($1.59 \cdot 10^{-2}\,\mathrm{m^2\,s^{-2}}$). The distribution of the anomalies (Figure 2.4) for both $\overline{u'u'}$ and $\overline{v'v'}$ indicate that the phase of the seasonal cycle depends on the location. This is particularly evident comparing the patterns of MAM and SON which have an absolute pattern correlation of less than 0.26 for $\overline{u'u'}$ and $\overline{v'v'}$.

As for the long-term mean, $\overline{u'v'}$ show a different behaviour. The maximum deviations from the long term mean are less in boreal winter and spring compared to summer and fall, as depicted in Figure 2.5. Obviously $\overline{u'v'}$ does not show a distinct shift of its distribution with the seasons but more a broadening towards the summer. From Figure 2.4 emerges no clear pattern which

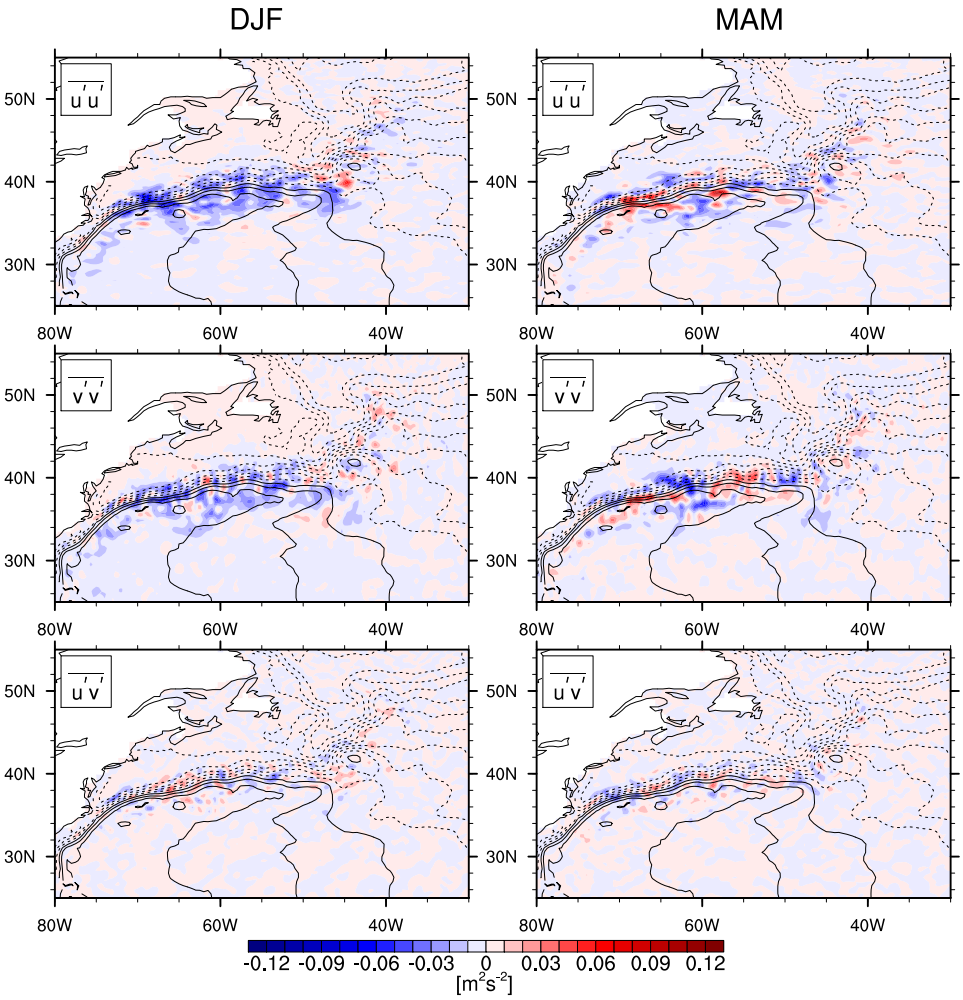

Figure 2.4: *Anomalous Reynolds stress terms with respect to the long-time mean for the seasons DJF (left panels) and MAM (right panels). Mean dynamic ocean topography from Niiler et al. (2003) is contoured at an interval of* 10 cm *to indicate the mean flow.*

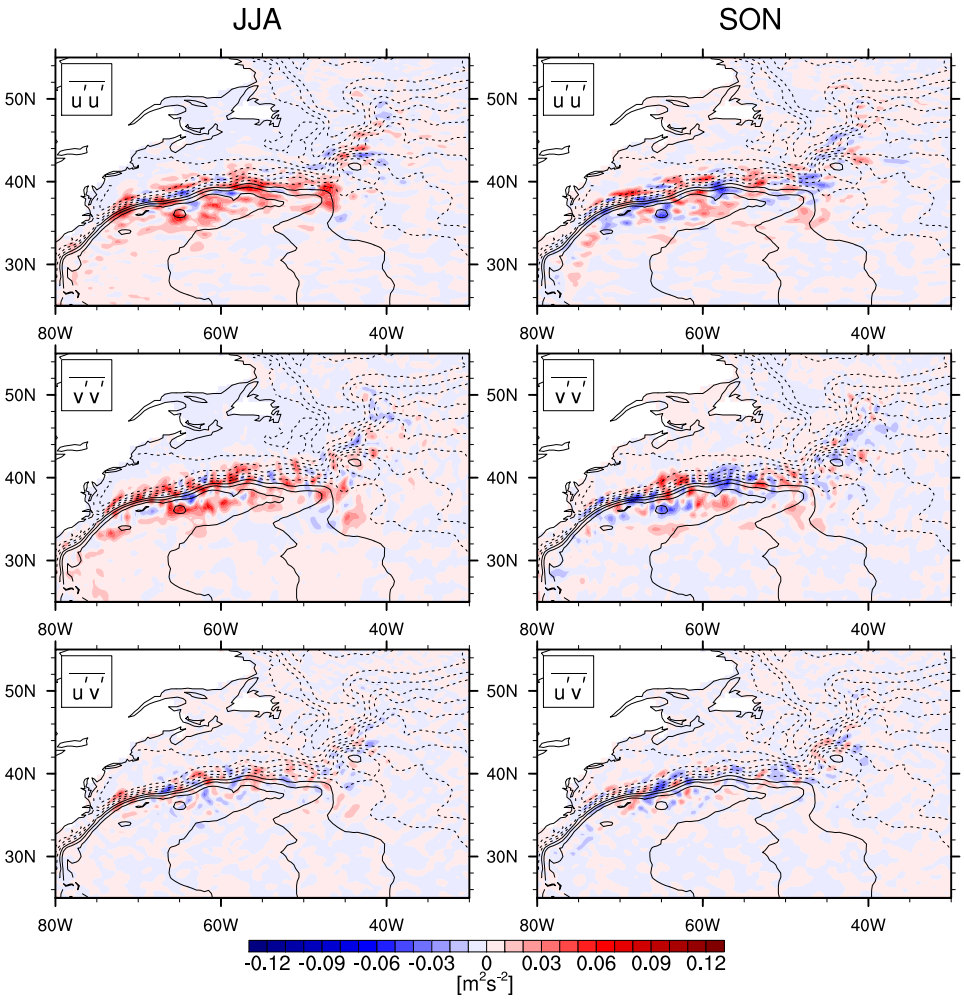

Continued Figure 2.4: *Same for seasons JJA (left panels) and SON (right panels).*

Quantity		Average	STD	Minimum	Maximum
DJF	$\overline{u'u'}$	$-1.04 \cdot 10^{-2}$	$1.59 \cdot 10^{-2}$	$-8.99 \cdot 10^{-2}$	$6.58 \cdot 10^{-2}$
	$\overline{v'v'}$	$-7.48 \cdot 10^{-3}$	$1.41 \cdot 10^{-2}$	$-8.96 \cdot 10^{-2}$	$6.40 \cdot 10^{-2}$
	$\overline{u'v'}$	$-5.58 \cdot 10^{-4}$	$8.74 \cdot 10^{-3}$	$-4.68 \cdot 10^{-2}$	$5.37 \cdot 10^{-2}$
MAM	$\overline{u'u'}$	$-2.36 \cdot 10^{-3}$	$1.75 \cdot 10^{-2}$	$-7.00 \cdot 10^{-2}$	$1.03 \cdot 10^{-1}$
	$\overline{v'v'}$	$-2.81 \cdot 10^{-3}$	$1.70 \cdot 10^{-2}$	$-8.22 \cdot 10^{-2}$	$9.45 \cdot 10^{-2}$
	$\overline{u'v'}$	$-8.12 \cdot 10^{-4}$	$9.03 \cdot 10^{-3}$	$-4.93 \cdot 10^{-2}$	$4.16 \cdot 10^{-2}$
JJA	$\overline{u'u'}$	$1.03 \cdot 10^{-2}$	$1.90 \cdot 10^{-2}$	$-6.37 \cdot 10^{-2}$	$1.23 \cdot 10^{-1}$
	$\overline{v'v'}$	$8.77 \cdot 10^{-3}$	$1.80 \cdot 10^{-2}$	$-5.30 \cdot 10^{-2}$	$1.06 \cdot 10^{-1}$
	$\overline{u'v'}$	$1.90 \cdot 10^{-3}$	$1.10 \cdot 10^{-2}$	$-5.54 \cdot 10^{-2}$	$5.68 \cdot 10^{-2}$
SON	$\overline{u'u'}$	$2.34 \cdot 10^{-3}$	$1.71 \cdot 10^{-2}$	$-6.10 \cdot 10^{-2}$	$9.24 \cdot 10^{-2}$
	$\overline{v'v'}$	$1.44 \cdot 10^{-3}$	$1.74 \cdot 10^{-2}$	$-7.08 \cdot 10^{-2}$	$9.66 \cdot 10^{-2}$
	$\overline{u'v'}$	$-5.36 \cdot 10^{-4}$	$1.07 \cdot 10^{-2}$	$-5.85 \cdot 10^{-2}$	$5.54 \cdot 10^{-2}$

Table 2.1: *Statistics for seasonal anomalous Reynolds stress terms in the area* 34°N *to* 42°N *and* 75°W *to* 47°W *(black box drawn in Figure 2.2). All quantities have units of* $\mathrm{m}^2\,\mathrm{s}^{-2}$*. Area weighting is applied for the average and standard deviation (STD) calculations.*

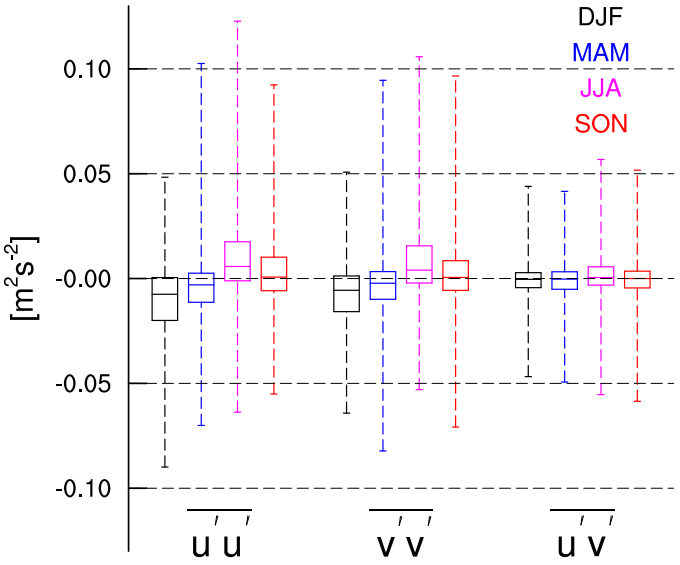

Figure 2.5: *Box plot statistic of seasonal anomalous Reynolds stress terms for the same region as in Table 2.1. The box extends from the* 25^{th} *to the* 75^{th} *percentile with the median shown as a band. The whiskers represent the maximum and minimum values.*

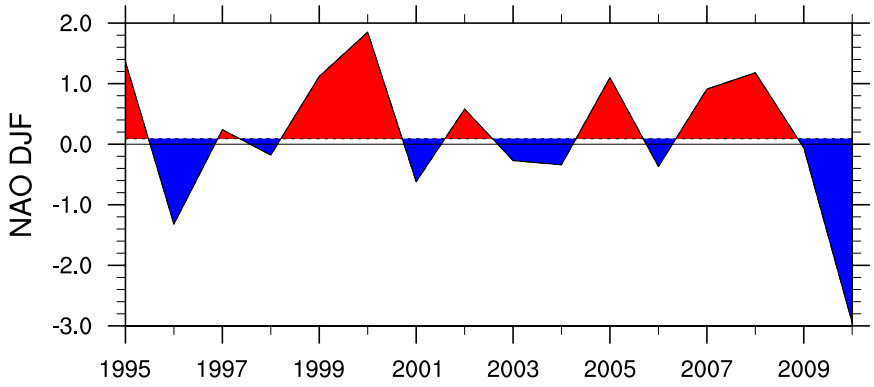

Figure 2.6: *The PC based DJF NAO index (see Section 2.1) for the winters with available satellite-derived velocity data. The dotted horizontal line is the median of the printed time series (0.09) and areas above (below) are shaded in red (blue). The DJF values of each winter are centred on January the 15^{th}.*

would allow any conclusions about the flux of zonal momentum in a zonally integrated sense.

2.2.3 Interannual Variability

For the time period of satellite-derived velocity data, the NAO shows a rather positive phase, shown in Figure 2.6, although the median is only marginally positive with a value of 0.09. The three products of DJF velocity anomalies are binned according to the winters listed in Table 2.2 and then averaged over each bin to obtain the Reynolds stress terms. The anomalies of these terms with respect to the overall DJF mean is shown in Figure 2.7. In contrast to the seasonal anomalies, the interannual anomalies of $\overline{u'u'}$ and $\overline{v'v'}$ do not show such a homogeneous pattern but a rather irregular one. As shown in Figure 2.8 (left panel) both of these tend to higher values in the area between the NES and the Grand Banks of Newfoundland (labeled as DOWN) during a positive state of the NAO. This leads to higher values of EKE (i.e. $\frac{1}{2}\left(\overline{u'u'} + \overline{v'v'}\right)$) associated with an positive NAO phase in this region. Between Cape Hatteras and the NES (labeled as UP) the distribution of $\overline{u'u'}$ and $\overline{v'v'}$ is somewhat broader. Here the distributions are not shifted with respect to the phase of the NAO but the skewness of the distributions differs. During a positive (negative) phase of the NAO the skewness of $\overline{u'u'}$, $\overline{v'v'}$ and EKE is positive (negative), hence lower (higher) values for these quantities are more likely. This is an indication for the regional dependency of the response of mesoscale turbulent motion to interannual atmospheric variability.

The possible impact of the NAO is more clear for the $\overline{u'v'}$ term, as depicted in Figure 2.8 (right panel). The dipole structure of positive values upstream and negative values downstream of the NES is present for both

Phase	Winter			
NAO+	94'/95'	96'/97'	98'/99'	99'/00'
	01'/02'	04'/05'	06'/07'	07'/08'
NAO-	95'/96'	97'/98'	00'/01'	02'/03'
	03'/04'	05'/06'	08'/09'	09'/10'

Table 2.2: *Winters associated with a positive or negative NAO, based on the median of the time series shown in Figure 2.6.*

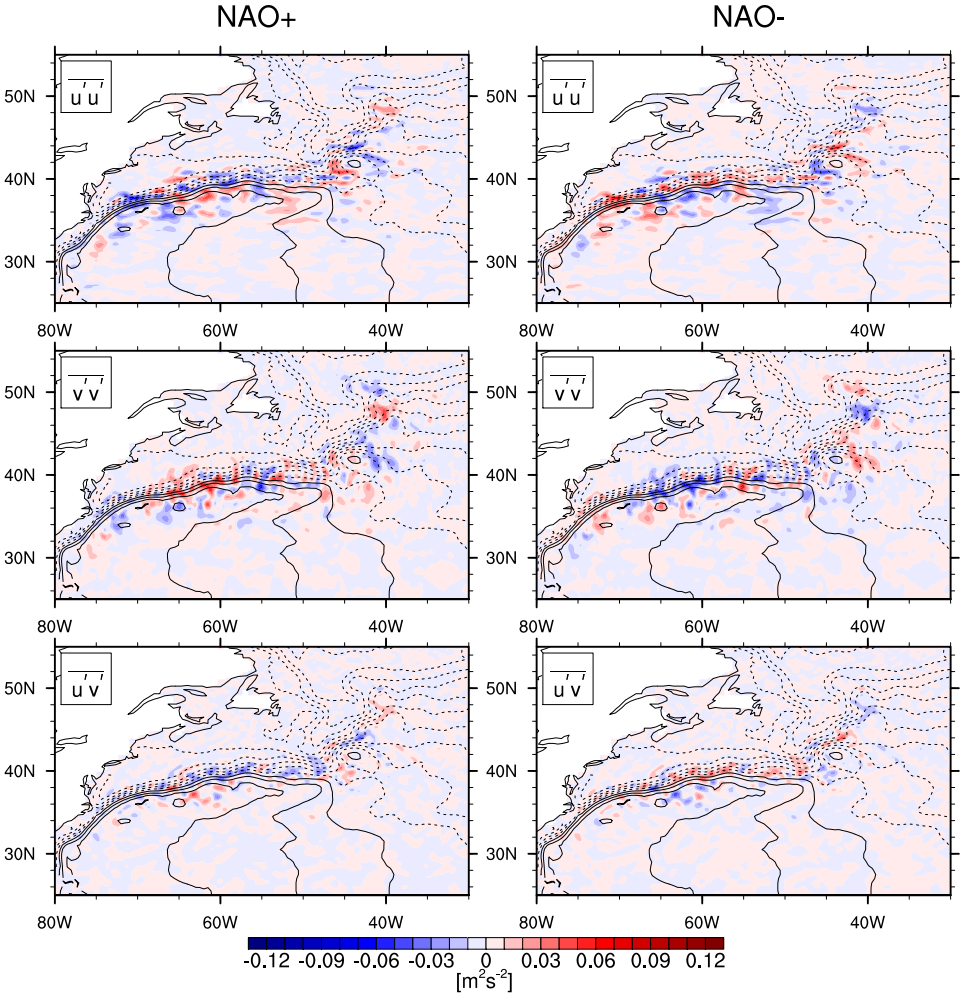

Figure 2.7: *Same as Figure 2.4 but for Reynolds stress terms associated with positive (left panels) and negative (right panels) NAO as anomalies of DJF mean.*

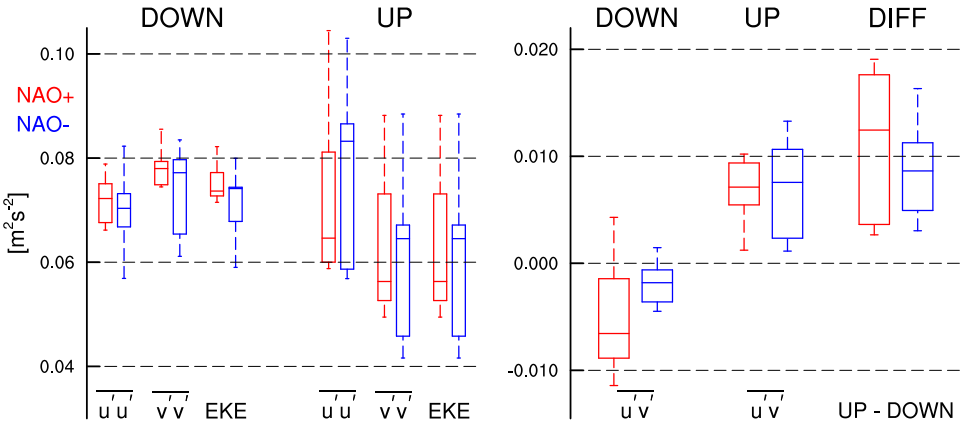

Figure 2.8: *Box plot of area-averaged Reynolds stress terms and EKE from each contributing winter of NAO+ (red) and NAO- (blue). The areas over which are averaged are upstream (UP) and downstream (DOWN) the NES (see Figure 2.2). Also shown is the difference of the area-averaged* $\overline{u'v'}$ *terms. Downstream of the NES there is a shift of the distributions of both* $\overline{u'u'}$ *and* $\overline{v'v'}$ *towards more positive values during positive NAO winters. Upstream of the NES the skewness of the distributions appears to be affected.* $\overline{u'v'}$ *reveals once again the dipole structure with positive values UP and negative values DOWN, but with an increased dipole strength for NAO+.*

phases of the NAO. But for negative phases the dipole tends to have a smaller range due to a shift and reduction of variability of the distribution on the downstream side whereas the range tends to be larger during a positive NAO event. For all three terms the influence of the NAO is much more pronounced downstream of the NES. Since all patterns associated with the seasonal cycle (Figure 2.4), as well as the interannual variability imprinted on the DJF field (Figure 2.7), are of the same order of magnitude compared to the long-term mean (Figure 2.3), it can be expected that both variabilities have an measurable influence on the transport driven by EMF convergence. Together with the impact on the dipole strength, this emphasizes the importance of the NAO on the velocity covariance and therefore the strength of the recirculation gyres. The question of how the recirculation is actually influenced is not easy to answer at this point. But the tendency of increased absolute cross-stream gradient of $\overline{u'v'}$ during a positive NAO phase is indicated by negative anomalies north of the mean current axis and positive south of it, as depicted by Figure 2.7. Hence a strengthening of momentum flux into the jet can be proposed. The model described in the next section will help to shed light on the question of what kind and how strong the influence will be.

Chapter 3

The Model

The goal of this chapter is to formulate a simple linear shallow water model including realistic sea floor topography and driven by the turbulent flux of momentum derived from satellite measurements. This makes it possible to hindcast transport induced by eddies and therefore examine their effect on both the mean state and the variability of the circulation.

3.1 The Governing Equations

To get a formulation of the governing equations representing the influence of the eddy momentum flux on the barotropic mean transport, consider the momentum and continuity equation of an incompressible Boussinesq ocean

$$\rho_0 \left(\frac{D\boldsymbol{u}}{Dt} + \boldsymbol{f} \times \boldsymbol{u} \right) = -\nabla p \tag{3.1a}$$

$$\nabla \cdot \boldsymbol{u} = 0 \tag{3.1b}$$

where ρ_0 is the fluid reference density, $\boldsymbol{u} = (u, v, w)$ the fluid velocity, $\boldsymbol{f} = f\,\boldsymbol{k}$ the Coriolis parameter in a vectorial representation, p the pressure and $\frac{D}{Dt} = \frac{\partial}{\partial t} + \boldsymbol{u} \cdot \nabla$ denominates the material derivative. Exploiting the rigid-lid approximation, the system fulfils the kinematic boundary conditions (BCs).

$$z = 0 \qquad w = 0 \tag{3.2a}$$

$$z = -H \qquad w = -(u\frac{\partial H}{\partial x} + v\frac{\partial H}{\partial y}) \tag{3.2b}$$

The rigid-lid approximation is valid for the barotropic mode if the length scale of motion is small compared to the radius of deformation and the time scale is longer than $\frac{1}{f}$. Since the surface signal of baroclinic internal waves is small compared to their signal in the interior (usually a factor of $1 \cdot 10^2$ to

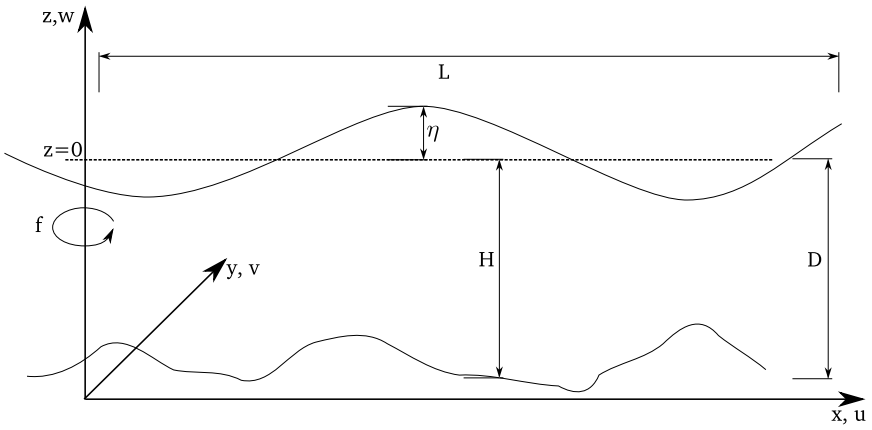

Figure 3.1: *Sketch of the domain*

$1 \cdot 10^3$) and very small compared to the surface signal of barotropic inertia-gravity waves, the rigid-lid approximation is also reasonable for the baroclinic modes.

Since the ocean is considered incompressible the advective term in the material derivative can be rewritten with help of the Einstein summation convention.

$$\boldsymbol{u} \cdot \nabla \boldsymbol{u} = u_j \frac{\partial}{\partial x_j} u_i = \frac{\partial}{\partial x_j} u_i u_j - u_i \frac{\partial}{\partial x_j} u_j = \frac{\partial}{\partial x_j} u_i u_j \tag{3.3}$$

3.1.1 Vertically and Reynolds-averaged Formulation

The first step to obtain the Reynolds-averaged momentum equations is to replace the dynamical variables by a long time average and its deviation, e.g. $\boldsymbol{u} = \overline{\boldsymbol{u}} + \boldsymbol{u}'$, where $(\bar{\cdot})$ denotes time average and again primes are used for anomalies. With use of (3.3), (3.1a) becomes

$$\rho_0 \left(\frac{\partial \boldsymbol{u}}{\partial t} + \frac{\partial}{\partial x_j} \left(\overline{u}_i \overline{u}_j + \overline{u}_i u_j' + u_i' \overline{u}_j + u_i' u_j' \right) + \boldsymbol{f} \times \boldsymbol{u} \right) = -\nabla p \tag{3.4}$$

The second step is time-averaging (3.4) over a period long enough for the primed quantities to average out

$$\rho_0 \left(\frac{\partial \overline{u}_i \overline{u}_j}{\partial x_j} + \frac{\partial \overline{u_i' u_j'}}{\partial x_j} + \boldsymbol{f} \times \overline{\boldsymbol{u}} \right) = -\nabla \overline{p} \tag{3.5}$$

where the ensemble rules of averaging are applied.[1]

$$\overline{\overline{a}} = \overline{a}$$
$$\overline{a+b} = \overline{a} + \overline{b}$$
$$\overline{a\overline{b}} = \overline{a}\overline{b}$$

Now consider motion with a small aspect ratio, i.e., $\delta = \frac{D}{L} \ll 1$, where D is the vertical and L the horizontal length scale. The equation of vertical momentum reduces to the hydrostatic approximation due to scaling arguments (see *Pedlosky*, 1987, Chapter 3.3), i.e., in its integral form

$$\overline{p} = -g \int_{-H}^{0} \overline{\rho}\, \mathrm{d}z + p_a \tag{3.6}$$

with g being the gravitational acceleration and p_a the atmospheric pressure. The effect of the atmosphere is discarded at this stage by assuming the atmospheric pressure to be constant and interpreting pressure as an anomaly from p_a.

Both (3.1b) and the horizontal components of (3.5) are averaged in the vertical (denoted by $\langle\cdot\rangle$). For the Reynolds stress terms in the horizontal momentum equation, use of Leibniz Integral Rule and (3.2) gives

$$\begin{aligned}
\left\langle \frac{\partial \overline{u_j' u_i'}}{\partial x_j} \right\rangle =& \frac{1}{H} \int_{-H}^{0} \frac{\partial \overline{u_j' u_i'}}{\partial x_j}\, \mathrm{d}z \\
=& \frac{1}{H} \left(\frac{\partial}{\partial x} \int_{-H}^{0} \overline{u' u_i'}\, \mathrm{d}z + \frac{\partial}{\partial y} \int_{-H}^{0} \overline{v' u_i'}\, \mathrm{d}z + [\,\overline{w' u_i'}\,]_{-H}^{0} \right. \\
& \left. - \frac{\partial H}{\partial x} \overline{u' u_i'}\,|_{z=-H} - \frac{\partial H}{\partial y} \overline{v' u_i'}\,|_{z=-H} \right) \\
=& \frac{1}{H} \left(\frac{\partial}{\partial x} \int_{-H}^{0} \overline{u' u_i'}\, \mathrm{d}z + \frac{\partial}{\partial y} \int_{-H}^{0} \overline{v' u_i'}\, \mathrm{d}z \right)
\end{aligned}$$

Likewise,

$$\left\langle \frac{\partial \overline{u}_j \overline{u}_i}{\partial x_j} \right\rangle = \frac{1}{H} \left(\frac{\partial}{\partial x} \int_{-H}^{0} \overline{u}\overline{u}_i\, \mathrm{d}z + \frac{\partial}{\partial y} \int_{-H}^{0} \overline{v}\overline{u}_i\, \mathrm{d}z \right)$$

[1] For time periods long enough, the time derivative vanishes, since

$$\overline{\frac{\partial \overline{\boldsymbol{u}} + \boldsymbol{u}'}{\partial t}} = \overline{\frac{\partial \boldsymbol{u}'}{\partial t}} = \frac{1}{t_2 - t_1} \int_{t_1}^{t_2} \frac{\partial \boldsymbol{u}'}{\partial t}\, \mathrm{d}t = \frac{\boldsymbol{u}'(t_2) - \boldsymbol{u}'(t_1)}{t_2 - t_1} \to 0 \text{ as } (t_2 - t_1) \to \infty$$

For the vertical average of the continuity equation (3.1b), Leibniz Integral Rule and (3.2) gives

$$\begin{aligned}
0 =& \int_{-H}^{0} \nabla \cdot \boldsymbol{u} \, \mathrm{d}z \\
=& \frac{\partial}{\partial x} \int_{-H}^{0} u \, \mathrm{d}z + \frac{\partial}{\partial y} \int_{-H}^{0} v \, \mathrm{d}z + [w]_{-H}^{0} - \frac{\partial H}{\partial x} u|_{z=-H} - \frac{\partial H}{\partial y} v|_{z=-H} \\
=& \frac{\partial}{\partial x} \int_{-H}^{0} u \, \mathrm{d}z + \frac{\partial}{\partial y} \int_{-H}^{0} v \, \mathrm{d}z
\end{aligned} \tag{3.7}$$

The divergence and the integral are linear operators, hence (3.7) applies to both $\overline{\boldsymbol{u}}$ and $\boldsymbol{u}'$ separately. Since time-averaging commute with the spatial derivatives and the depth integral, the time-averaged form of (3.7) evaluates to

$$0 = \frac{\partial}{\partial x} \int_{-H}^{0} \overline{u} \, \mathrm{d}z + \frac{\partial}{\partial y} \int_{-H}^{0} \overline{v} \, \mathrm{d}z = \frac{\partial H \langle \overline{u} \rangle}{\partial x} + \frac{\partial H \langle \overline{v} \rangle}{\partial y} \tag{3.8}$$

This equation basically tells us that the time mean horizontal volume transport is divergence free, which implies the existence of a barotropic transport streamfunction Ψ with

$$\frac{\partial \Psi}{\partial x} = H \langle \overline{v} \rangle \tag{3.9a}$$

$$\frac{\partial \Psi}{\partial y} = -H \langle \overline{u} \rangle \tag{3.9b}$$

With the aid of (3.6) the vertical average of the pressure gradient evaluates to

$$\begin{aligned}
\langle \nabla \overline{p} \rangle &= \frac{1}{H} \int_{-H}^{0} \nabla \overline{p} \, \mathrm{d}z = \frac{1}{H} \left[\nabla \int_{-H}^{0} \overline{p} \, \mathrm{d}z + \overline{p}_b \nabla H \right] \\
&= \frac{1}{H} \left[\nabla \left([z\overline{p}]_{-H}^{0} - \int_{-H}^{0} z \frac{\partial \overline{p}}{\partial z} \, \mathrm{d}z \right) - \overline{p}_b \nabla H \right] \\
&= \frac{1}{H} \left[\nabla \left(H \overline{p}_b + \rho_0 \overline{\Phi} \right) - \overline{p}_b \nabla H \right] \\
&= \nabla \overline{p}_b + \frac{\rho_0}{H} \nabla \overline{\Phi}
\end{aligned} \tag{3.10}$$

with p_b being the bottom pressure and $\Phi = \frac{g}{\rho_0} \int_{-H}^{0} z\rho \, \mathrm{d}z$ the potential energy per unit area.

Now (3.1) can be written in the vertically- and Reynolds-averaged form as follows

$$
\begin{aligned}
-f\,\langle\overline{v}\rangle = &-\frac{1}{\rho_0}\frac{\partial\overline{p}_b}{\partial x}-\frac{1}{H}\frac{\partial\overline{\Phi}}{\partial x}\\
&-\frac{1}{H}\left(\frac{\partial}{\partial x}\int_{-H}^{0}\overline{u'u'}\,\mathrm{d}z+\frac{\partial}{\partial y}\int_{-H}^{0}\overline{u'v'}\,\mathrm{d}z\right)-\left\langle\frac{\partial\overline{u}_j\overline{u}}{\partial x_j}\right\rangle \qquad (3.11a)\\
f\,\langle\overline{u}\rangle = &-\frac{1}{\rho_0}\frac{\partial\overline{p}_b}{\partial y}-\frac{1}{H}\frac{\partial\overline{\Phi}}{\partial y}\\
&-\frac{1}{H}\left(\frac{\partial}{\partial x}\int_{-H}^{0}\overline{u'v'}\,\mathrm{d}z+\frac{\partial}{\partial y}\int_{-H}^{0}\overline{v'v'}\,\mathrm{d}z\right)-\left\langle\frac{\partial\overline{u}_j\overline{v}}{\partial x_j}\right\rangle \qquad (3.11b)\\
0 = &\frac{\partial H\,\langle\overline{u}\rangle}{\partial x}+\frac{\partial H\,\langle\overline{v}\rangle}{\partial y} \qquad (3.11c)
\end{aligned}
$$

This set of equations can be interpreted as a linear topographic Shallow Water Model (SWM) in steady state driven by the vertically-averaged eddy momentum flux, advection by mean flow and the gradient of potential energy (cf. (3.16)). Therefore it presents a diagnostic set of equations for the depth-averaged flow.

3.1.2 Vorticity Equation

In order to get deeper insights of the dynamical processes, the vorticity equation is derived from (3.11). Multiplying the left hand side of (3.11a) and (3.11b) with $\frac{H}{H}$ and taking the curl leads to

$$
\begin{aligned}
H\,\langle\overline{v}\rangle\,\frac{\partial}{\partial y}\frac{f}{H}+H\,\langle\overline{u}\rangle\,\frac{\partial}{\partial x}\frac{f}{H}+\frac{f}{H}\left(\frac{\partial H\,\langle\overline{u}\rangle}{\partial x}+\frac{\partial H\,\langle\overline{v}\rangle}{\partial y}\right) &= \frac{\partial M}{\partial x}-\frac{\partial Z}{\partial y}\\
+\frac{\partial}{\partial y}\left\langle\frac{\partial\overline{u}_j\overline{u}}{\partial x_j}\right\rangle-\frac{\partial}{\partial x}\left\langle\frac{\partial\overline{u}_j\overline{v}}{\partial x_j}\right\rangle-\frac{\partial}{\partial x}\left(\frac{1}{H}\frac{\partial\overline{\Phi}}{\partial y}\right)+\frac{\partial}{\partial y}\left(\frac{1}{H}\frac{\partial\overline{\Phi}}{\partial x}\right) &\qquad (3.12)
\end{aligned}
$$

where Z is the zonal and M the meridional component of the eddy momentum flux forcing in (3.11a) and (3.11b). Since (3.11c) reveals that the vertically integrated time averaged flow field is non-divergent, there exists a volume transport streamfunction Applying this definition and (3.11c) to (3.12) lead to

$$
J(\Psi,\frac{f}{H})=\frac{\partial M}{\partial x}-\frac{\partial Z}{\partial y}+\frac{\partial}{\partial y}\left\langle\frac{\partial\overline{u}_j\overline{u}}{\partial x_j}\right\rangle-\frac{\partial}{\partial x}\left\langle\frac{\partial\overline{u}_j\overline{v}}{\partial x_j}\right\rangle+J\left(\overline{\Phi},\frac{1}{H}\right) \qquad (3.13)
$$

where J is the Jacobian, i.e., $J(A,B)=\frac{\partial A}{\partial x}\frac{\partial B}{\partial y}-\frac{\partial A}{\partial y}\frac{\partial B}{\partial x}$. This equation is the topographic Sverdrup Balance, driven by the curl of vertically averaged eddy momentum flux, the advection term arising from the mean flow and

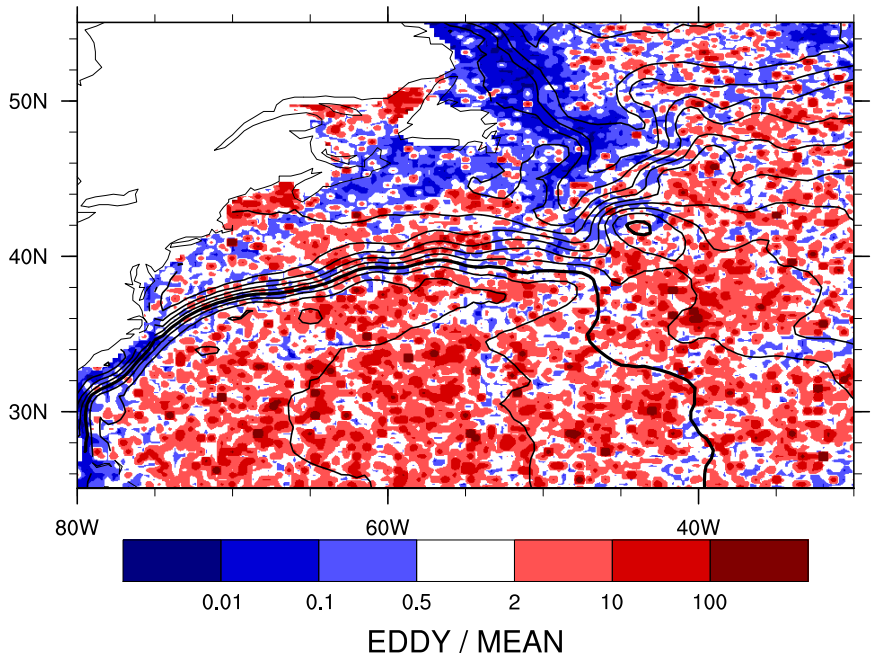

Figure 3.2: *Estimate of the absolute ratio of contribution to the local vorticity budged by the curl of the EMF (EDDY) and the advection of relative vorticity by the mean flow (MEAN). Both quantities are calculated at the surface from satellite-derived surface velocity values (Le Traon et al., 1998). The mean dynamic ocean topography (Niiler et al., 2003) is contoured with an interval of* 10 cm *to map the path of the mean flow.*

the Joint Effect of Baroclinicity and Relief (JEBAR) ($J(\overline{\Phi}, \frac{1}{H})$). The mean flow advection is of minor importance for the vorticity balance in most places compared to the EMF (see Figure 3.2), although not completely negligible. Since the vorticity balance is linear and the interest of this thesis is focused on the transport driven by the EMF, from now on the JEBAR term and the term arising from mean flow advection are not considered. Hence the resultant streamfunction only represents the transport driven by the curl of vertically averaged eddy momentum flux. However, the transport driven by the other terms can, in principle, be computed given the required data and the total transport evaluates as their sum.

The barotropic volume streamfunction can be evaluated by integrating the right hand side of (3.13) along lines of constant $\frac{f}{H}$ from the equator at the eastern boundary (*Mellor et al.*, 1982; *Greatbatch et al.*, 1991). In other words, the curl of the forcing pushes transport over lines of constant planetary PV. Since Ψ is evaluated by integrating along lines of constant PV, the influence on transport is of non-local character.

3.1.3 Shallow Water Model

Bathymetry is an important agent for depth integrated transport driven by wind stress. The bottom pressure torque arising from pressure differences over topographic features has been shown to balance the meridional mass transport of western boundary currents along the continental slope. This allows a coherent conceptual framework for all wind driven ocean currents without the need to consider viscous effects (*Hughes and de Cuevas*, 2001). However, dissipation is still needed due to both numerical and physical reasons. Isolated features as seamounts or small islands with steep sloping topography tend to trap energy by resonating with barotropic Rossby waves (*Rhines*, 1969). Since no process in the model is so far capable of dissipating this accumulated wave energy, additional damping has to be introduced. This damping can be achieved, among others, by two different kinds of parameterisations: vertical mixing of momentum represented by bottom friction and horizontal mixing of momentum represented using a viscosity. To reduce the computational effort and to keep the model linear, only the linear formulation of bottom stress is considered, i.e.,

$$\frac{\boldsymbol{\tau_b}}{\rho_0} = r\boldsymbol{u} \tag{3.14}$$

with the bottom stress $\boldsymbol{\tau_b} = (\tau_b^\lambda, \tau_b^\theta)$ and r being the linear friction coefficient. Further applying all simplifications mentioned in Section 3.1.2, (3.11) reduces to

$$-f\langle\overline{v}\rangle = -\frac{1}{\rho_0}\frac{\partial\overline{p}_b}{\partial x} + Z - \frac{r}{H}\langle\overline{u}\rangle \tag{3.15a}$$

$$f\langle\overline{u}\rangle = -\frac{1}{\rho_0}\frac{\partial\overline{p}_b}{\partial y} + M - \frac{r}{H}\langle\overline{v}\rangle \tag{3.15b}$$

$$0 = \frac{\partial H\langle\overline{u}\rangle}{\partial x} + \frac{\partial H\langle\overline{v}\rangle}{\partial y} \tag{3.15c}$$

To take into account the effects of sphericity, the system will be expressed in spherical coordinates. In order to obtain a solution of (3.15) for a given eddy momentum flux, an iterative approach is performed and the resulting time dependent SWM (3.16)[2] is run to steady state.

$$\frac{\partial u}{\partial t} - fv = -\frac{g}{a\cos\theta}\frac{\partial\eta}{\partial\lambda} + Z - \frac{r}{H}u \tag{3.16a}$$

$$\frac{\partial v}{\partial t} + fu = -\frac{g}{a}\frac{\partial\eta}{\partial\theta} + M - \frac{r}{H}v \tag{3.16b}$$

$$0 = \frac{\partial\eta}{\partial t} + \frac{1}{a\cos\theta}\left[\frac{\partial Hu}{\partial\lambda} + \frac{\partial\cos\theta Hv}{\partial\theta}\right] \tag{3.16c}$$

[2]For the sake of readability the chevrons and overbars are droped from now on.

where $g\eta = \frac{p_b}{\rho_0}$, θ is latitude, λ is longitude, a is the radius of the Earth and Z and M are the zonal and meridional component of the forcing by the eddy momentum flux (3.17), but now expressed in spherical coordinates[3]. Since surface velocities, derived from altimeter measurements by satellite, are used to estimate $\overline{u'u'}$, $\overline{u'v'}$ and $\overline{v'v'}$, a vertical profile has to be assumed to be able to integrate the fluxes vertically. *Wunsch* (1997) pointed out, that a large fraction of EKE in the GSER has an equivalent barotropic vertical structure, hence a linearly decreasing profile[4] is chosen.

$$Z = -\frac{1}{2Ha\cos\theta}\left[\frac{\partial}{\partial\lambda}\left(H\,\overline{u'u'}\,|_s\right) + \frac{\partial}{\partial\theta}\left(\cos\theta H\,\overline{u'v'}\,|_s\right)\right] \tag{3.17a}$$

$$M = -\frac{1}{2Ha\cos\theta}\left[\frac{\partial}{\partial\lambda}\left(H\,\overline{u'v'}\,|_s\right) + \frac{\partial}{\partial\theta}\left(\cos\theta H\,\overline{v'v'}\,|_s\right)\right] \tag{3.17b}$$

Here $\overline{u'u'}\,|_s$, $\overline{v'v'}\,|_s$ and $\overline{u'v'}\,|_s$ are the Reynolds stress components at the surface.

3.2 Numerics

In contrast to most of the modern atmospheric general circulation models (AGCMs) using spherical harmonics, ocean models are often defined on finite grids. Spatial as well as temporal derivatives are approximated by truncating the Taylor expansion and therefore are expressed by finite differences. Two possible sources of error arise: the round-off error due to limited precision of the computing environment and the truncation error. However, the latter can be made arbitrarily small by reducing the step size in both the spatial and the temporal dimension. Unfortunately, this neither guarantees convergence nor stability of the scheme used (*Mesinger and Arakawa*, 1976). The following sections will contain all prerequisites to render (3.16) in a convergent and stable finite difference form.

3.2.1 Grid

As stated by *Mesinger and Arakawa* (1976), the C-grid (see Figure 3.3) is the best spatial arrangement of the variables when using centred differences, since all inertia-gravity waves have group velocities with correct sign, provided that the grid spacing Δ is smaller than the radius of deformation R, i.e.

$$R = \frac{c}{f} > \Delta \tag{3.18}$$

[3] Actually only the horizontal dimensions are transformed to spherical coordinates while the vertical component is still written in Cartesian coordinates. The effects of curvature of the layer of interest can safely be neglected, since $\max\{H\} \ll a$.

[4] The chosen shape function alters only the amplitude and not the distribution of the forcing field, in the case that the profile is self-similar everywhere.

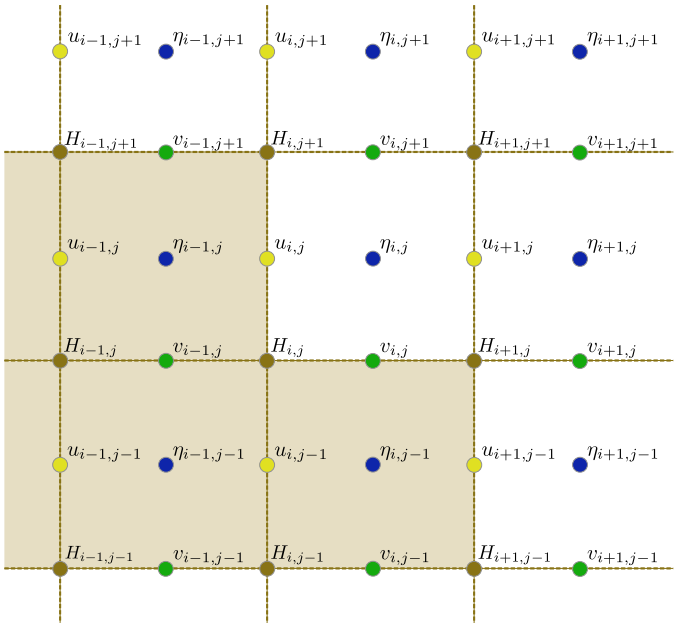

Figure 3.3: *Sketch of grid staggering. Actually, this is the C-Grid as defined by Mesinger and Arakawa (1976) but with topography included. The light brown patch illustrates the representation of coastlines. All variables on land and coastline are confined to zero value.*

with shallow water phase velocity $c = \sqrt{gH}$. In the interior of the basin, R is very large for the barotropic mode ($\sim 20°$ for $H = 4000\,\mathrm{m}$), hence this criteria is not very stringent. Since the model should take bathymetry into account, the classical C-grid is enhanced with a additional grid having its nodes located at the centres of the η-grid boxes to store topographic information. This information is then interpolated on the various grids by averaging[5]. The surface Reynolds stresses are provided to the model on the H-grid and are interpolated by a four-point average onto the η-grid to assist the evaluation of the spatial derivatives in (3.17), hence its finite difference

[5]Two-point averaging for the u- and v-grid and a four-point average for the η-grid.

form is

$$Z|_u^{i,j} = -\frac{1}{2\,H|_u^{i,j}\,a\cos\theta|_u^j}\left(\frac{\overline{u'u'}\,|_\eta^{i,j}\;H|_\eta^{i,j} \;-\; \overline{u'u'}\,|_\eta^{i-1,j}\;H|_\eta^{i-1,j}}{\Delta\lambda}\right.$$
$$\left.+\frac{\cos\theta|_H^{j+1}\;\overline{u'v'}\,|_H^{i,j+1}\;H|_H^{i,j+1} \;-\; \cos\theta|_H^{j}\;\overline{u'v'}\,|_H^{i,j}\;H|_H^{i,j}\;)}{\Delta\theta}\right) \tag{3.19a}$$

$$M|_v^{i,j} = -\frac{1}{2\,H|_v^{i,j}\,a\cos\theta|_v^j}\left(\frac{\overline{u'v'}\,|_H^{i+1,j}\;H|_H^{i+1,j} \;-\; \overline{u'v'}\,|_H^{i,j}\;H|_H^{i,j}\;)}{\Delta\lambda}\right.$$
$$\left.+\frac{\cos\theta|_\eta^{j}\;\overline{v'v'}\,|_\eta^{i,j}\;H|_\eta^{i,j} \;-\; \cos\theta|_\eta^{j-1}\;\overline{v'v'}\,|_\eta^{i,j-1}\;H|_\eta^{i,j-1}}{\Delta\theta}\right) \tag{3.19b}$$

where the notation $A|_b^{i,j}$ is introduced to denominate quantity A at the i-th and j-th node of grid b.

3.2.2 Boundary Conditions

The basin boundary is determined by topography, i.e., all points having a depth less or equal to zero are considered as land. Likewise, all points on the u- and v-grid situated between two land points and all points on the η-grid surrounded by four land points on the H-grid are also considered as land. The boundary condition

$$\boldsymbol{n}\cdot\boldsymbol{u} = 0 \text{ at the boundary} \tag{3.20}$$

is satisfied, since the coastline is solely located on velocity grid points representing the normal velocity (see Figure 3.3). The model initially sets these velocities to zero and does not consider them while integrating in time.

3.2.3 Time Stepping Scheme

There are various time stepping schemes, whose application depends on the problem under consideration. Since this model should properly represent inertia-gravity waves, the scheme of *Heaps* (1971) is used. It has the great advantage of presenting the wave equation in a very natural form on a C-grid. The only change made in this work is using a implicit backward instead of a trapezoidal scheme for the friction term. Now (3.16) can be written in

its finite differenced form

$$\begin{aligned}
\eta|_{\eta}^{i,j,l+1} =& \eta|_{\eta}^{i,j,l} \\
&- \frac{\Delta t}{a\cos\,\theta|_{\eta}^{j}\,\Delta\theta}\left(\,H|_{v}^{i,j+1}\,\cos\,\theta|_{v}^{j+1}\,v|_{v}^{i,j+1,l}\,-\,H|_{v}^{i,j}\,\cos\,\theta|_{v}^{j}\,v|_{v}^{i,j,l}\,\right) \\
&- \frac{\Delta t}{a\cos\,\theta|_{\eta}^{j}\,\Delta\lambda}\left(\,H|_{u}^{i+1,j}\,u|_{u}^{i+1,j,l}\,-\,H|_{u}^{i,j}\,u|_{u}^{i,j,l}\,\right) \qquad (3.21a)\\
u|_{u}^{i,j,l+1} =& \frac{1}{1+\frac{\Delta tr}{H|_{v}^{i,j}}}\Bigg[\,u|_{u}^{i,j,l}\,+\Delta t f\,v|_{u}^{i,j,l} \\
&- \frac{\Delta t\,g}{a\cos\,\theta|_{u}^{j}\,\Delta\lambda}\left(\,\eta|_{\eta}^{i,j,l+1}\,-\,\eta|_{\eta}^{i-1,j,l+1}\,\right)+\Delta t\,Z|_{u}^{i,j}\,\Bigg] \qquad (3.21b)\\
v|_{v}^{i,j,l+1} =& \frac{1}{1+\frac{\Delta tr}{H|_{v}^{i,j}}}\Bigg[\,v|_{v}^{i,j,l}\,-\Delta t f\,u|_{v}^{i,j,l+1} \\
&- \frac{\Delta t\,g}{a\Delta\theta}\left(\,\eta|_{\eta}^{i,j,l+1}\,-\,\eta|_{\eta}^{i,j-1,l+1}\,\right)+\Delta t\,M|_{v}^{i,j}\,\Bigg] \qquad (3.21c)
\end{aligned}$$

where the superscript l labels the time step, i.e $t = l\Delta t$.

3.2.4 Convergence and Stability

The most important criterion for convergence, the Courant–Friedrichs–Lewy (CFL) condition, gives a upper bound on the time step Δt.

$$\Delta t < \frac{\Delta x}{c} = \frac{a\Delta\lambda\cos\theta_{max}}{\sqrt{gH}} \qquad (3.22)$$

Another criterion arising from the Coriolis term is

$$\Delta t < \left|\frac{1}{f}\right| = \frac{R}{c} \qquad (3.23)$$

which is less stringent than the CFL criterion as long as (3.18) is satisfied. The third criterion is due to the linear friction used in the model and demands that the grid resolves the Stommel-layer width, which leads to a lower bound of the friction parameter

$$r > a\cos\theta\Delta\lambda H\beta \qquad (3.24)$$

with $\beta = \frac{1}{a}\frac{\partial f}{\partial\theta}$.

3.3 Domain

The domain extends from 100°W to 0°E and 15°N to 55°N, which ensures that the region of interest is sufficiently far away from the boundary. A zonal

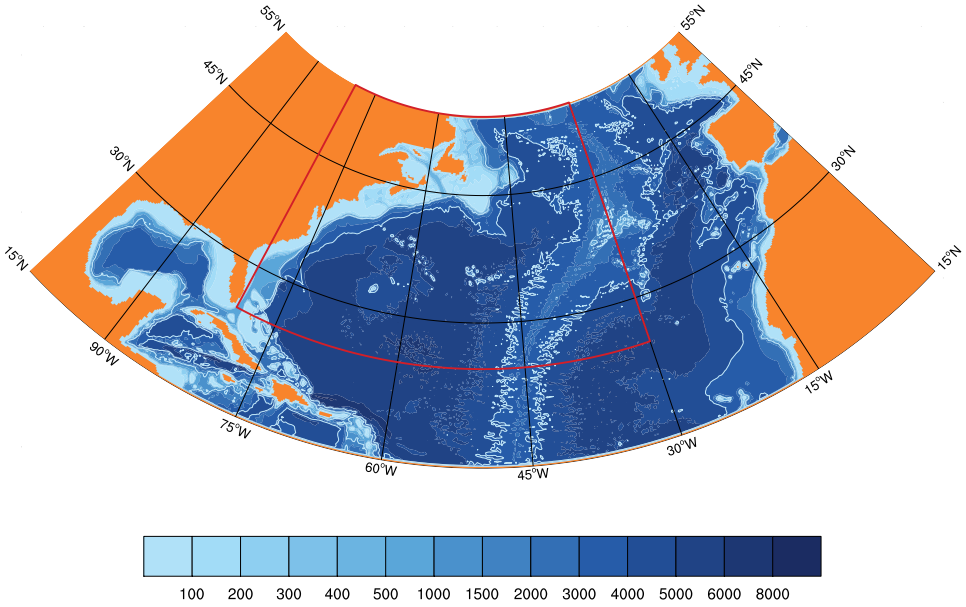

Figure 3.4: *Domain used by the model. Coastline and bathymetry are taken from ETOPO1 with additional coastlines at the northern and southern edge. The red box indicates the location of the GSER and all results are plotted for this area only. The two grey contours indicate the* 1500 m *and* 4000 m *isobath.*

Quantity	Threshold	Used by model	Criteria Eqn.
$\Delta\lambda, \Delta\theta$	$< 2.73°$	$1/6°$	(3.18)
Δt	< 53.23 s	20 s	(3.22)
r	$> 3.14{\cdot}10^{-3}$ m/s	$4{\cdot}10^{-3}$ m/s	(3.24)

Table 3.1: *Summary of threshold values for the parameters arising from stability and convergence criteria. Also listed are the values actually used by the model.*

and meridional grid resolution of $\frac{1}{6}^\circ$ is chosen to satisfy (3.18) and to resolve the spatial structure of the forcing. Both the coastline and solid boundaries at the edge of the domain are defined as the outermost lying H-grid points confining the basin (see Figure 3.4). This ensures the conservation of volume and momentum since there are no fluxes across the boundary. Bathymetry is taken from the ETOPO1 Ice Surface data set (*Amante and Eakins*, 2009). This global relief model of the Earth surface includes the top of the Antarctic and Greenland ice sheets and has a horizontal resolution of 1 arc-minute. The bathimetry is averaged onto the H-grid applying area-weighting. To reduce computational costs, only the contiguous water body of the NA is considered[6]. All above mentioned considerations are taken into account for the choice of the parameters listed in Table 3.1.

[6]Thanks to Willi Rath for providing the algorithm of identifying contiguous patches

Chapter 4

Results

This chapter presents the results of the model experiments. The experiments are distinguished only by the choice of forcing, which is described in Chapter 2. Each of the following sections will cover one set of experiments: the mean state, seasonal variability and wintertime variability associated with the NAO.

4.1 Mean State

This section summarises to a large extent the results already published by *Greatbatch et al.* (2010b). The barotropic streamfunction, produced by the model using the mean Reynolds stress forcing, is presented in Figure 4.1. The plot shows a cyclonic recirculation gyre north and an anticyclonic gyres south of the mean GS axis, where the northern gyre is confined by the Newfoundland Ridge to the east and the continental shelf to the north. These gyres resemble the observed recirculation gyres (*Schmitz*, 1980; *Hogg et al.*, 1986) and match the schematic barotropic recirculation, drawn by *Hogg* (1992) (see Figure 4.2), very well. Their shape is also in good agreement with the eddy-driven transport streamfunction presented by *Zhai et al.* (2004). The transport associated with the gyres exceed 50 Sv, reaching up to 120 Sv for the northern recirculation gyre (NRG), and hence can explain the observed increase of barotropic transport in the GSER (*Richardson*, 1985; *Hogg*, 1992; *Johns et al.*, 1995). It should be noted at this point that the magnitude of modelled transport is sensitive to the choice of the vertical profile of the Reynolds stresses. A profile which would confine the EMF more to the surface would lead to less transport, but its spatial distribution would not substantially change. East of the Newfoundland Ridge, the NAC is also enhanced and deflected by several gyres including the Mann eddy (*Mann*, 1967), although slightly shifted to the north-east compared to its surface signature found in the product of *Niiler et al.* (2003), and the circulation at the northwest corner (*Lazier*, 1994).

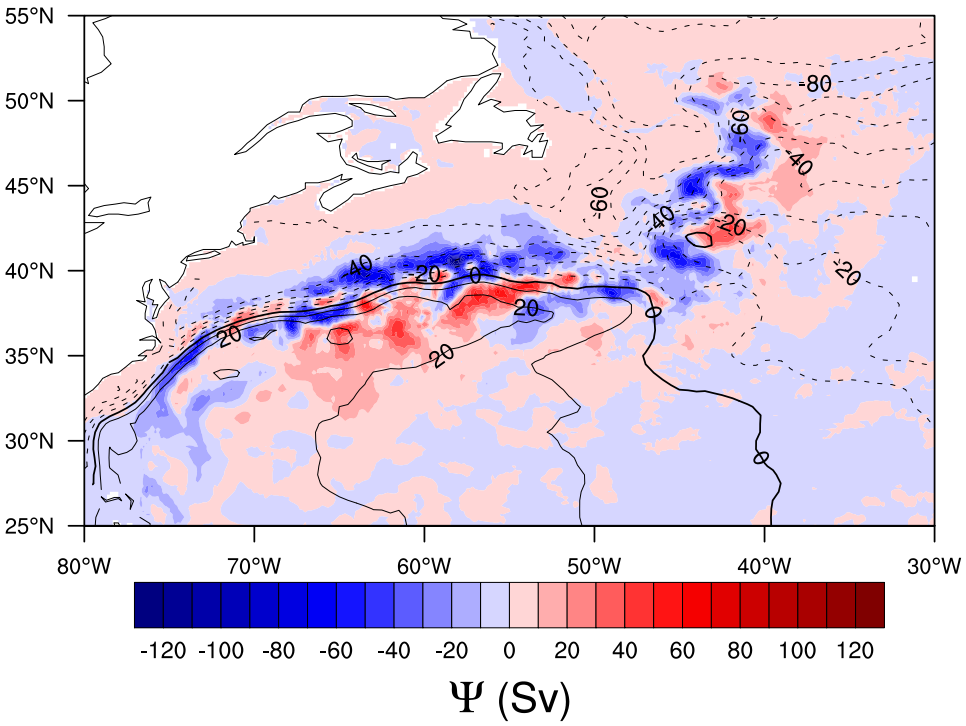

Figure 4.1: *Barotropic transport streamfunction* Ψ *in units of Sverdrup associated with the long-term mean Reynolds stress (see Section 2.2.1). The region downstream the NES and upstream the Newfoundland Ridge is characterised by a cyclonic gyre north of the mean Stream axis and a anticyclonic gyre south of it. Also visible is the anticyclonic Mann eddy (Mann, 1967). The mean dynamic ocean topography (Niiler et al., 2003) is contoured with an interval of* 10 cm *to indicate the mean axis of the GS.*

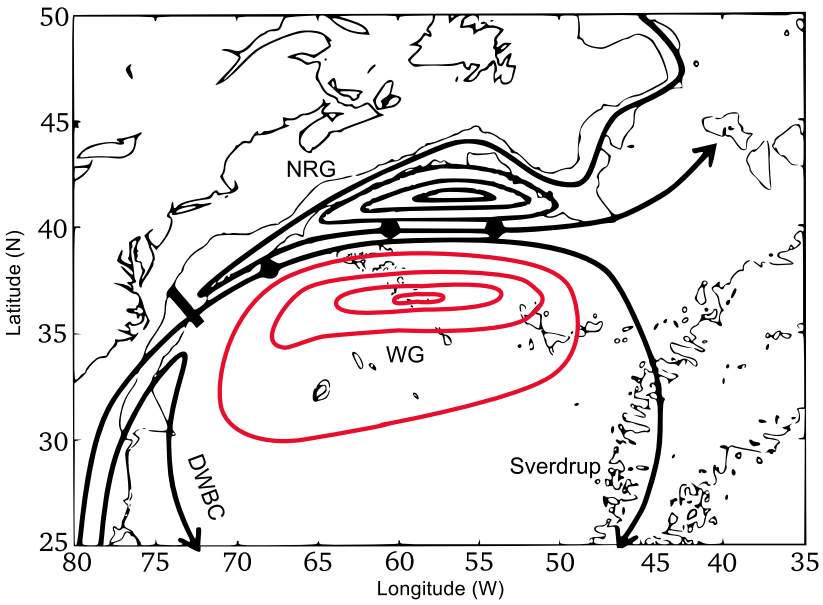

Figure 4.2: *Schematic streamfunction of the recirculation gyres in the GSER (Hogg, 1992, reprint of his Figure 10).*

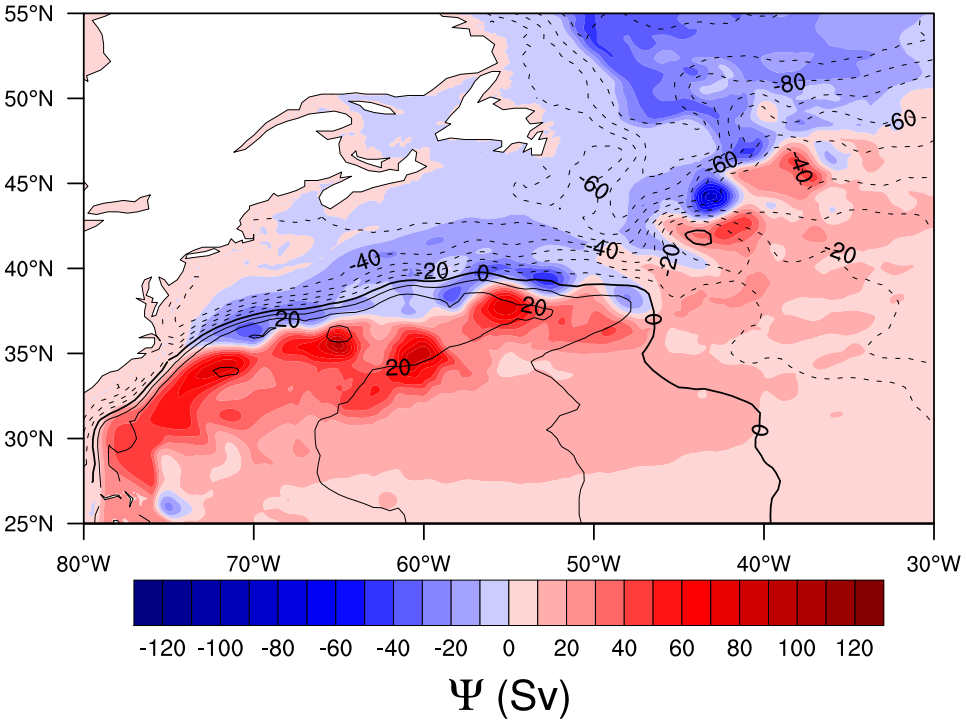

Figure 4.3: *Same as Figure 4.1, but for the barotropic streamfunction produced by the model of Smith et al. (2000). The figure is taken from Bryan et al. (2007, their Figure 4(c)).*

Most ocean general circulation models (OGCMs) do have difficulties to represent the dynamics of the GSER with desirable accuracy, although increasing resolution generally improves the picture (*Chassignet and Garraffo*, 2001). The barotropic streamfunction of a 1/10° eddy-permitting basin scale OGCM (*Smith et al.*, 2000), published by *Bryan et al.* (2007), is shown in Figure 4.3. It was forced with realistic surface winds and the mean circulation in the GSER is in good agreement with observations. This includes the location of the separation point near Cape Hatteras, the current speed and cross-stream structure and the position of the NAC with its meanders and troughs. The magnitude and geographical distribution of EKE and surface height anomalies are also well captured. However, the mean path of the GS seems to be shifted southwards between the separation point and the Newfoundland Ridge and the separation of the NAC at the northwest corner is displaced to the north west (*Smith et al.*, 2000). The streamfunctions of both the *Smith et al.* (2000) model and the linear SWM do show remarkable similarities especially downstream from the NES. They share anticyclonic recirculation cells located at 55°W, 61°W and 65°W on the southern flank of the current and a cyclonic cell, which extends from 50°W to at least 67°W on the northern side of the GS. Also the circulation patterns in the vicinity of the NAC, like the Mann eddy and the northwest corner, are in considerable good agreement. The noticeable correspondence of both model results supports the assumption of a strong projection of EMF forcing on the barotropic mode and hence an important influence of bottom topography. Since the SWM is solely driven by EMF convergence, this is a strong indication for the importance of Reynolds stresses for the mean barotropic transport and the recirculation in the GSER, at least in the *Smith et al.* (2000) model. There are, however, two regions where both models show distinct differences: upstream the NES on the warm flank of the GS and at about 45°W, where the current bends around the Newfoundland Ridge and turns to the north as the NAC. These two regions are locations where the local vorticity budget is likely to be dominated by advection of mean relative vorticity, instead of the curl of EMF convergence (see Figure 3.2). Especially upstream of the NES also the JEBAR term is important for the vorticity balance (*Greatbatch et al.*, 1991). Hence the disagreement in barotropic transport is not surprising.

4.2 Seasonal Variability

The seasonal variability of the GS transport has been studied from observations with various techniques. *Fu et al.* (1987) used the difference of sea level, derived from along-track altimeter data, at both sides of the current and found a seasonal cycle with a maximum in April. Also based on satellite altimetry, *Kelly and Gille* (1990) computed zonal geostrophic velocity pro-

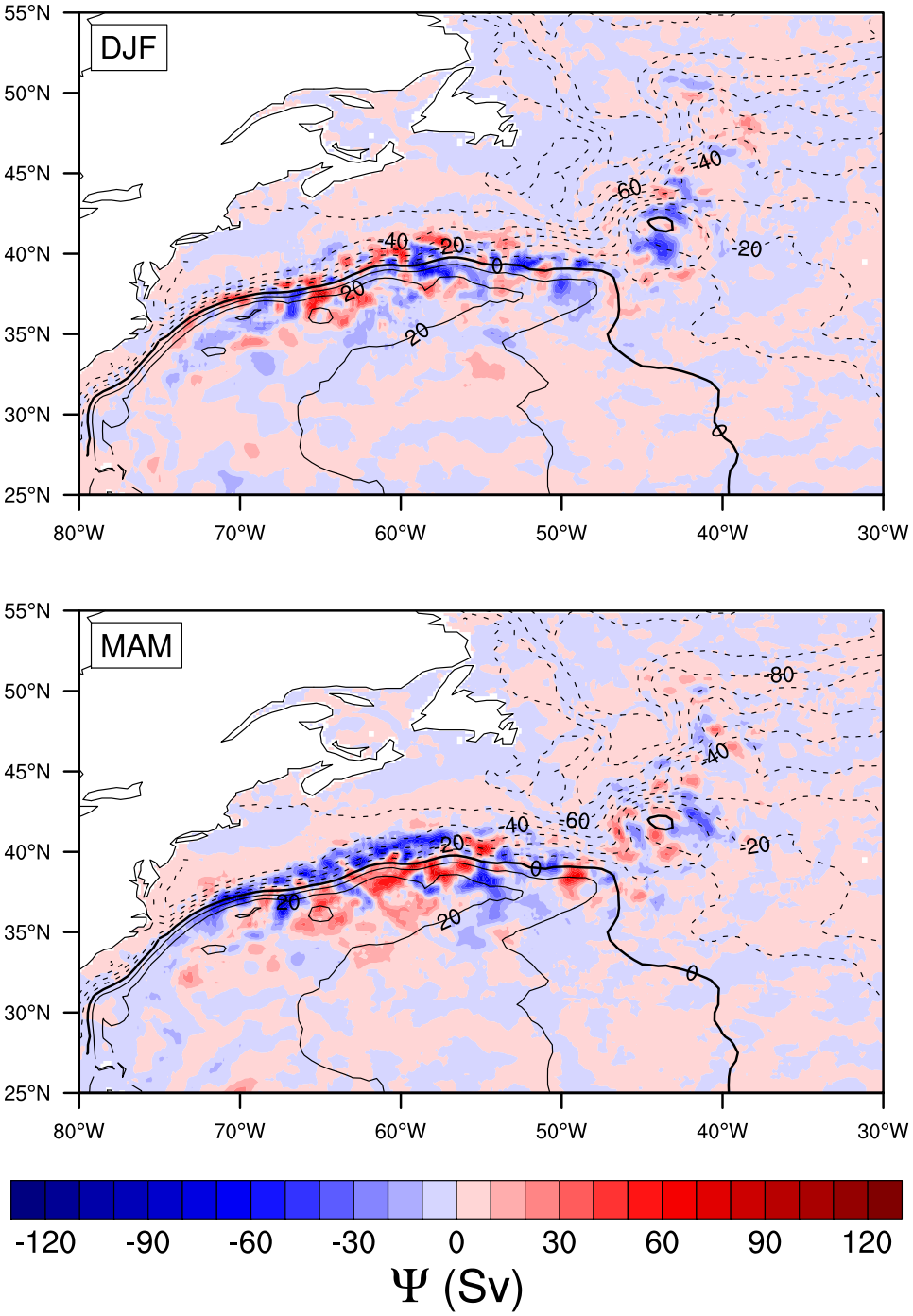

Figure 4.4: *Seasonal barotropic streamfunction anomaly for the seasons DJF, MAM, JJA and SON. Contours of the mean dynamic ocean topography (Niiler et al., 2003) are overlayed with a contour interval of* 10 cm.

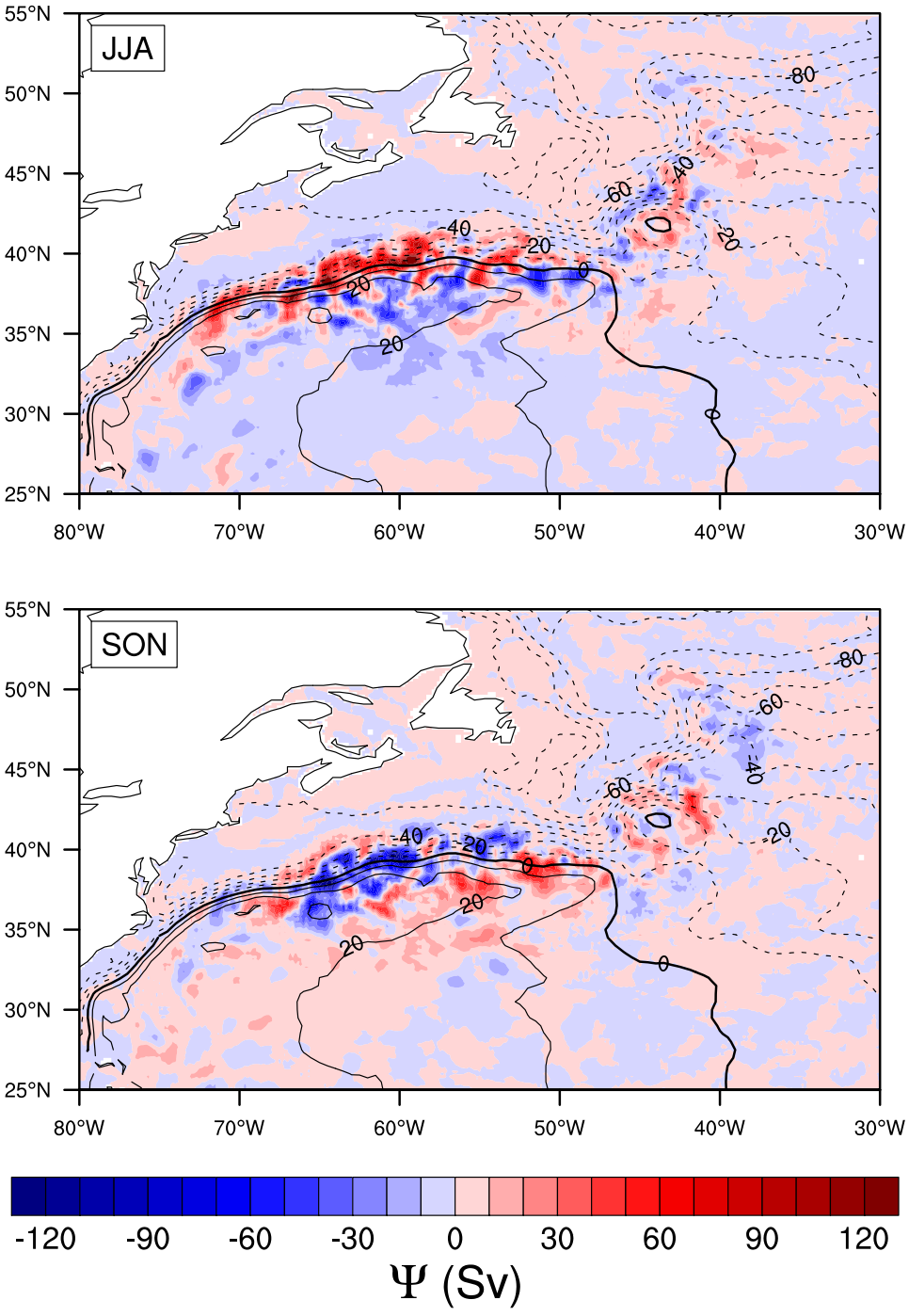

Continued Figure 4.4

files and derived the annual cycle of surface transport with a minimum in spring and a maximum in late fall. Using Acoustic Doppler Current Profiler (ADCP) measurements, *Rossby et al.* (2010) found a seasonal cycle of near surface transport with a maximum in the second half of the year. All of those studies where located upstream of the NES and their disagreement suggests either a rather small scale spatial structure of the seasonal variability or the results may not be statistically significant due to noise. The seasonal variation of transport due to the seasonal cycle of the EMF as produced by the model is show in Figure 4.4. The magnitude of local transport variation is comparable to the annual mean transport, which can not only be explained by meridional shifts of the recirculation cells but also by a seasonal intensification of these cells. However, the patterns of seasonal variation are of high spatial variance and no clear large scale annual pattern emerges from Figure 4.4.

The winter season (DJF) shows a rather noisy pattern with larger values upstream of the NES. The comparison of zonally averaged meridional bands of transport streamfunction, having a width of 4° and shown in Figure 4.5, supports the impression of an overall similar circulation to the annual mean during this season. The MAM anomaly pattern (Figure 4.4, Panel 2) exhibits a much more regular distribution with pronounced relative northern and southern recirculation cells at longitudes from 70°W to 55°W. The absolute streamfunction sections reveal, if any, only weak strengthening of the absolute circulation upstream of the NES. However, there is a significant[1] deepening of the cyclonic recirculation cell south of the mean flow at 70°W acting to decelerate the mean flow. At 60°W the northern recirculation appears to be enhanced together with a broadening of the easterly flow at the location of the annual mean GS path. This feature appears to be significantly different from the DJF season (see Figure 4.6), especially south of the currents mean path, and therefore suggests an increased and northerly shifted transport. Further downstream at 55°W the southerly anticyclonic gyre appears to be squeezed, while the northern gyre remains nearly unchanged compared to DJF, which leads to a sharpening of the westerly jet. However, this mean sharpening is a result of enhanced interannual variability south of the mean current during this season and is not related to a systematic shift of the MAM ensemble distribution at latitudes of about 38°N. Interestingly, the JJA anomaly pattern shows a reversal of sign compared to MAM (Figure 4.4, Panel 3). Again, upstream of 55°W the variation seems to be rather cross-stream, while further downstream it is of a more along-stream nature. The intensification of the anticyclonic recirculation cell at longitudes from 70°W to 60°W at the latitude of the mean jet axis (Figure 4.5)

[1] In this paragraph mean streamfunction profiles lying outside of the ensemble standard deviation envelope of the previous seasons profile, shown in Figure 4.6, are assumed to be significant.

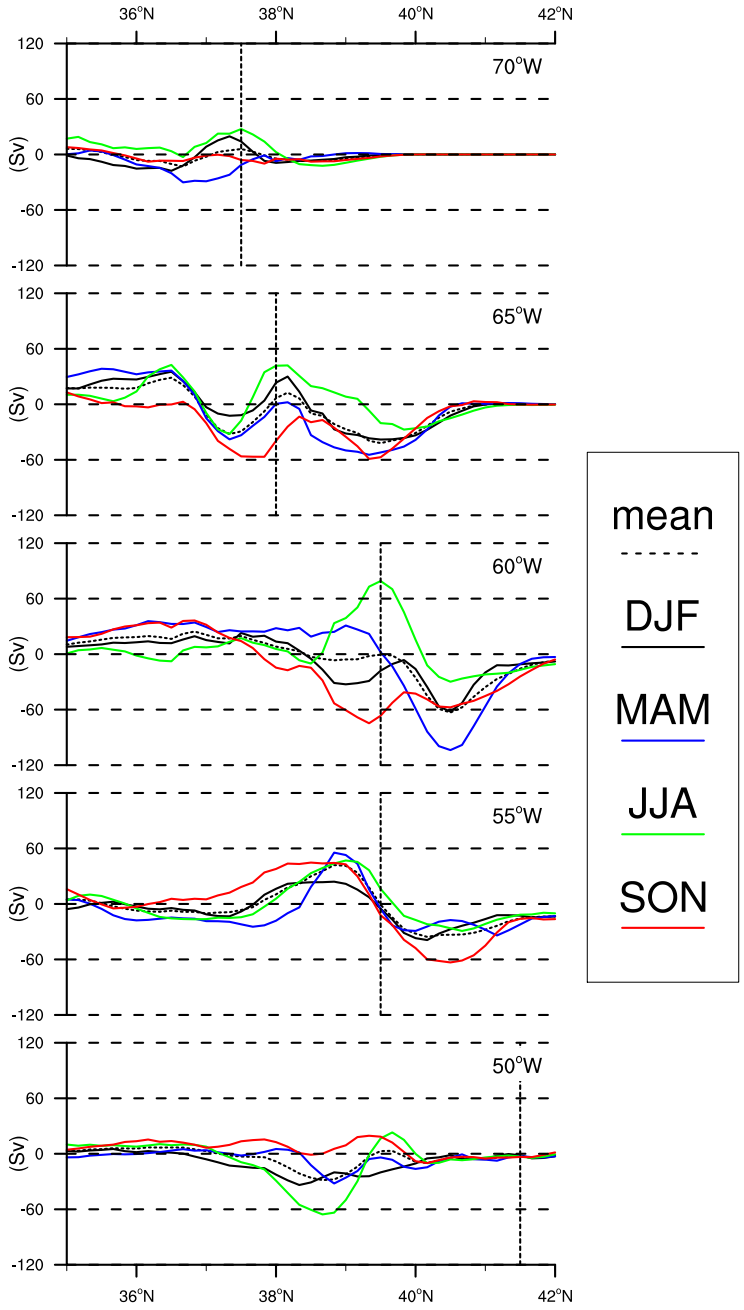

Figure 4.5: *Five meridional sections of the seasonal barotropic streamfunctions averaged over a meridional band of 4° width centred at the longitude used as panel label. The streamfunction of the annual mean transport is shown as the dotted black line and the position of the GS axis, defined here as the location of maximal negative meridional derivative of sea surface height (Nüiler et al., 2003), is marked as the vertical dashed black line. Eastward (westward) transport is indicated by a negative (positive) meridional gradient.*

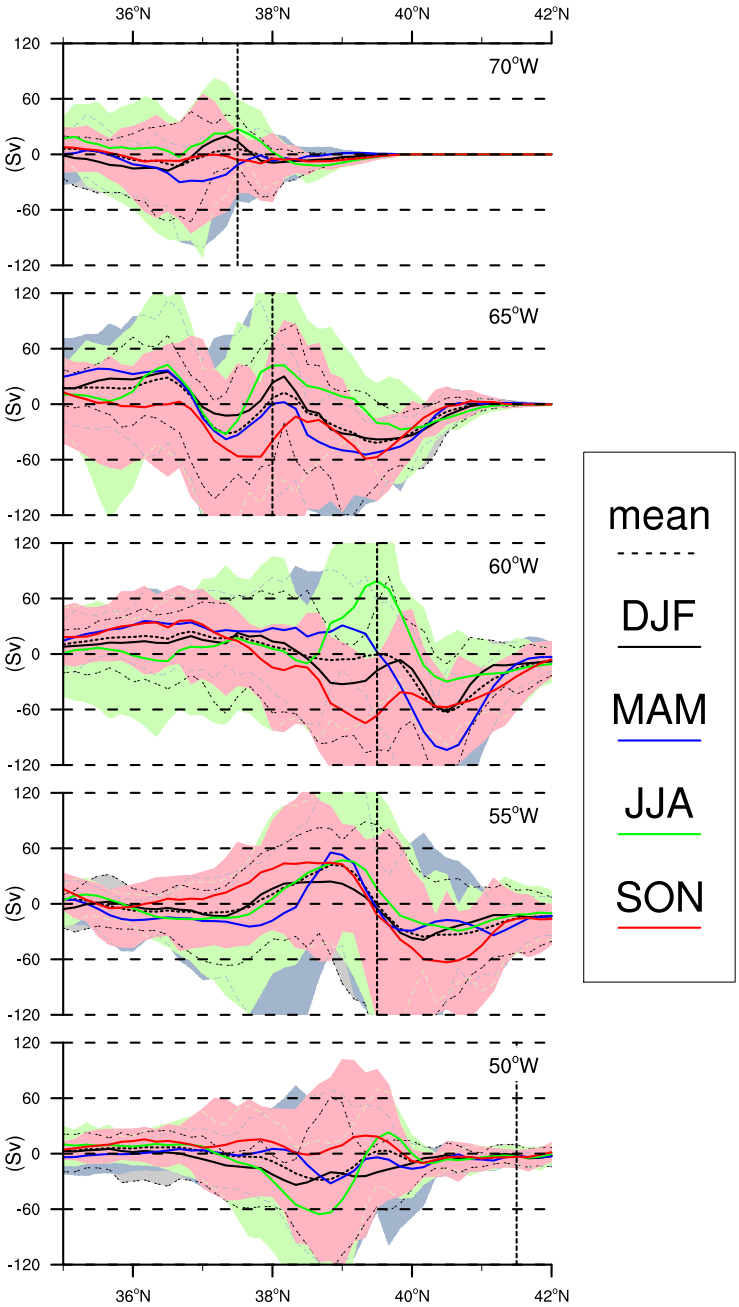

Figure 4.6: *Same as Figure 4.5, but with the ensemble spread as envelopes. The ensembles are the samples of all corresponding seasons, hence each contains 16 members. The envelopes extend from the $16^{th}$to the 84^{th}percentile which is about the same as the standard deviation of a normally distributed sample. The envelopes are confined by dashed lines of corresponding colour.*

indicates a seasonal shift of the mean jet axis to the north, which appears to be significant and is consistent with findings from inverted echo sounder measurements by *Tracey and Watts* (1986). This shift can also be observed at 55°W, although less pronounced and not significant. The anomaly pattern of SON (Figure 4.4, Panel 4) is characterised by a negative anomaly located at the NES and to some extent upstream of them. This anomaly is associated with a significant strengthening of the cyclonic recirculation cell located at 65°W and 60°W, where at the latter section the circulation seems to push the mean jet axis southward. At 55°W no lateral shift of the mean jet is suggested, since it is located between the circulation cells. At 50°W only in JJA the circulation does show considerable, however not significant, differences to the annual mean in the form of enhanced transport.

Downstream of the Newfoundland Ridge, the seasonal variations are of much smaller amplitude compared to the region upstream of it, although the annual mean transport is of similar magnitude at both sides of the ridge. This regional dependency of the strength of the seasonal signal is also evident for the individual Reynolds stress terms (see Figure 2.4) and hence is a consequence of a less pronounced seasonal EMF variability.

4.3 Variability associated with NAO

The structure of covariability of the Reynolds stresses with the NAO, investigated in Section 2.2.3, suggested a larger momentum flux convergence at the jet downstream of the NES and stronger recirculation during a positive phase of the NAO. The variability of the DJF transport as produced by the linear SWM is shown in Figure 4.7. Downstream the Newfoundland Ridge the signal of the NAO is less pronounced. The Mann eddy, slightly shifted eastward in the model world, seems to be strengthened and shifted to the north during a positive phase of the NAO. The northerly adjacent recirculation cells located in the NAC are weakened, while on the other hand the circulation in the vicinity of the northwest corner is strengthened. Furthermore, the seasonal DJF streamfunction appears to be quite robust, since both patterns associated with the NAO reproduce the DJF pattern quite well. The transport variability of the NAC recirculation associated with the NAO is more pronounced than the seasonal variability in this region, which might be an indication of the importance of interannual atmospheric variability for the circulation downstream the Newfoundland Ridge.

To draw a clearer picture for the GSER, the zonal averages of 4° meridional bands of the barotropic transport streamfunctions for DJF and the two phases of the NAO are plotted in Figure 4.8 at longitudes upstream the NES. Although both phases consists of only 50 % of the DJF data, their streamfunctions exhibit again remarkably similar profiles indicating a robust DJF signal. Their major difference to the mean DJF pattern is a northward

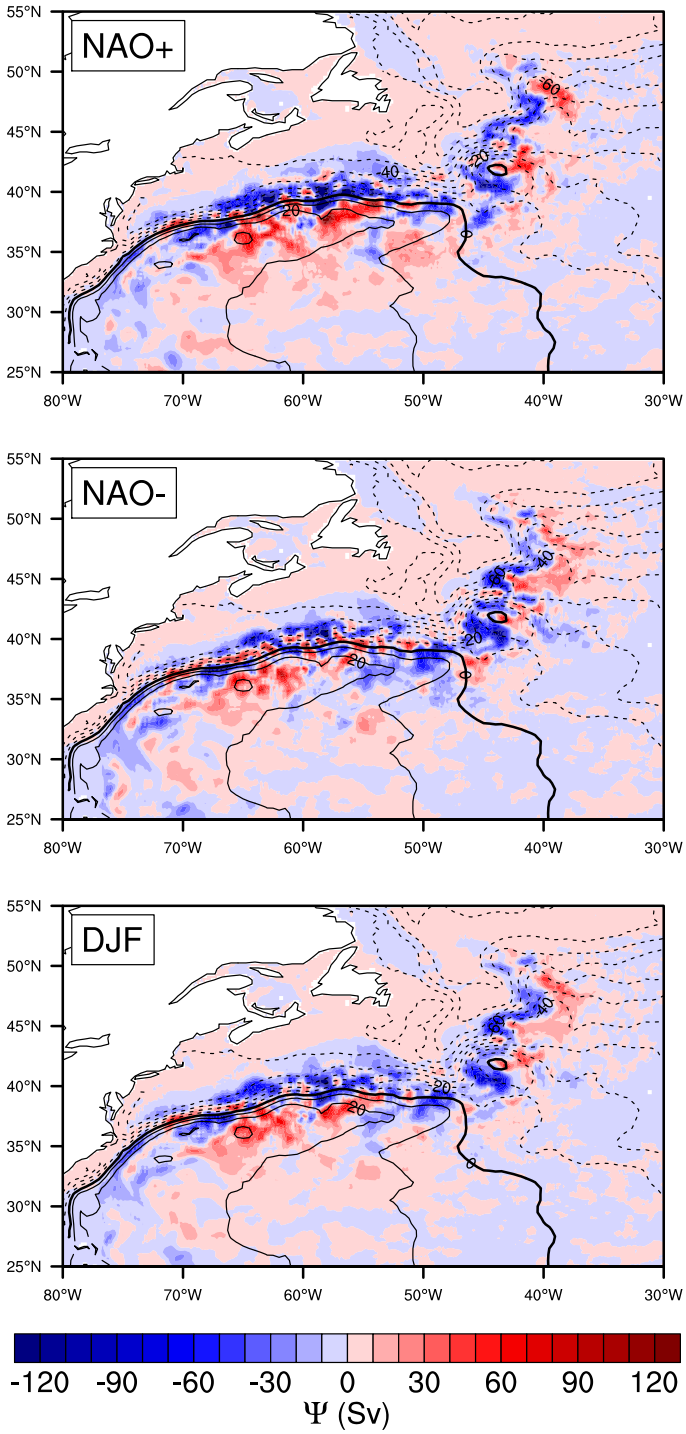

Figure 4.7: *Barotropic transport streamfunction of the DJF season separated according to the state of the NAO (first two panel) and the mean DJF streamfunction (bottom panel). Contour lines show the mean dynamic ocean topography (Niüler et al., 2003) with an interval of* 10 cm.

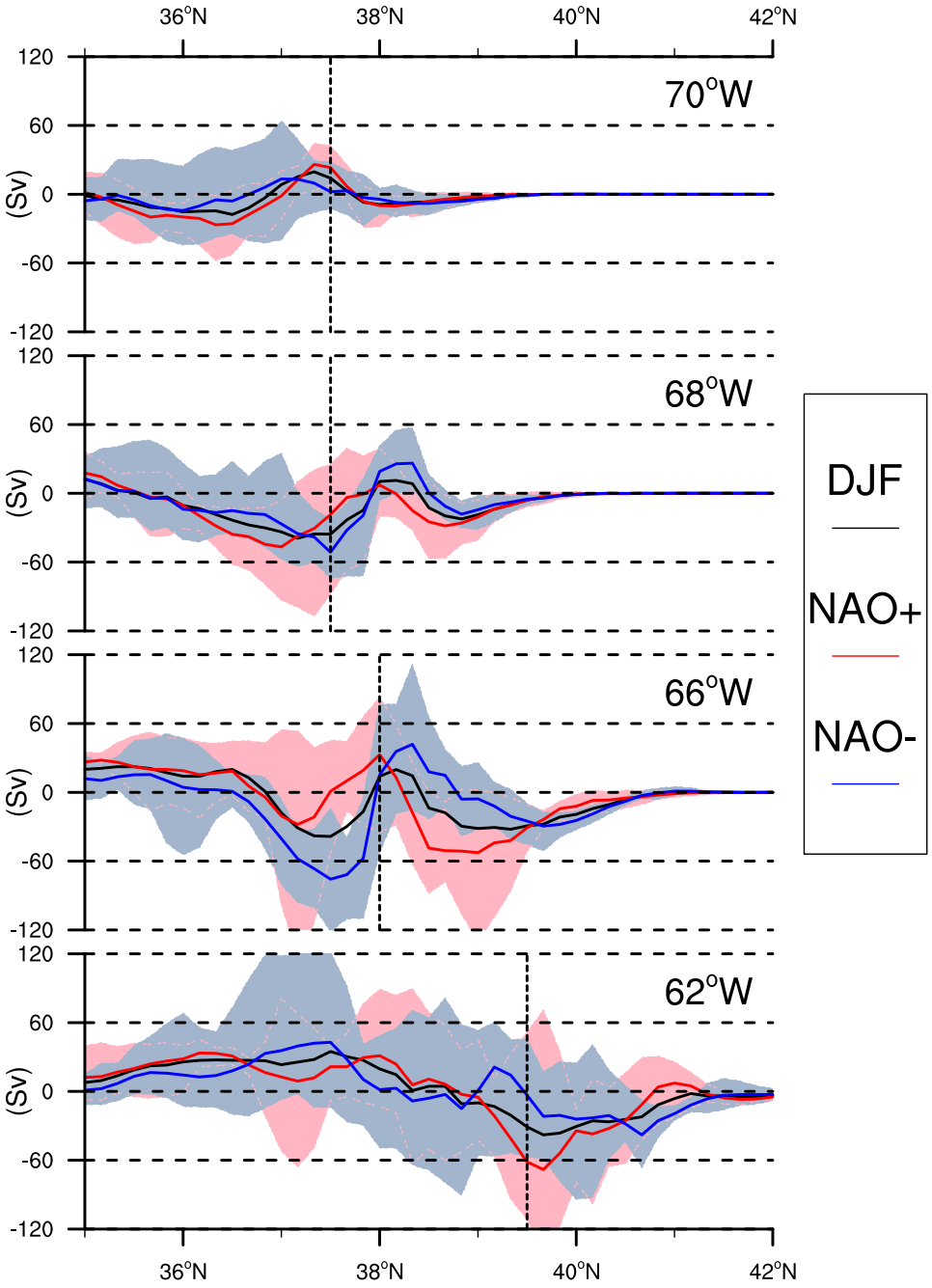

Figure 4.8: *Same as Figure 4.6 but for the DJF streamfunction and the variability associated with the NAO upstream the NES. The envelopes cover 68.75 % of the ensemble spread, where each ensemble consists of the DJF streamfunctions associated with one NAO phase.*

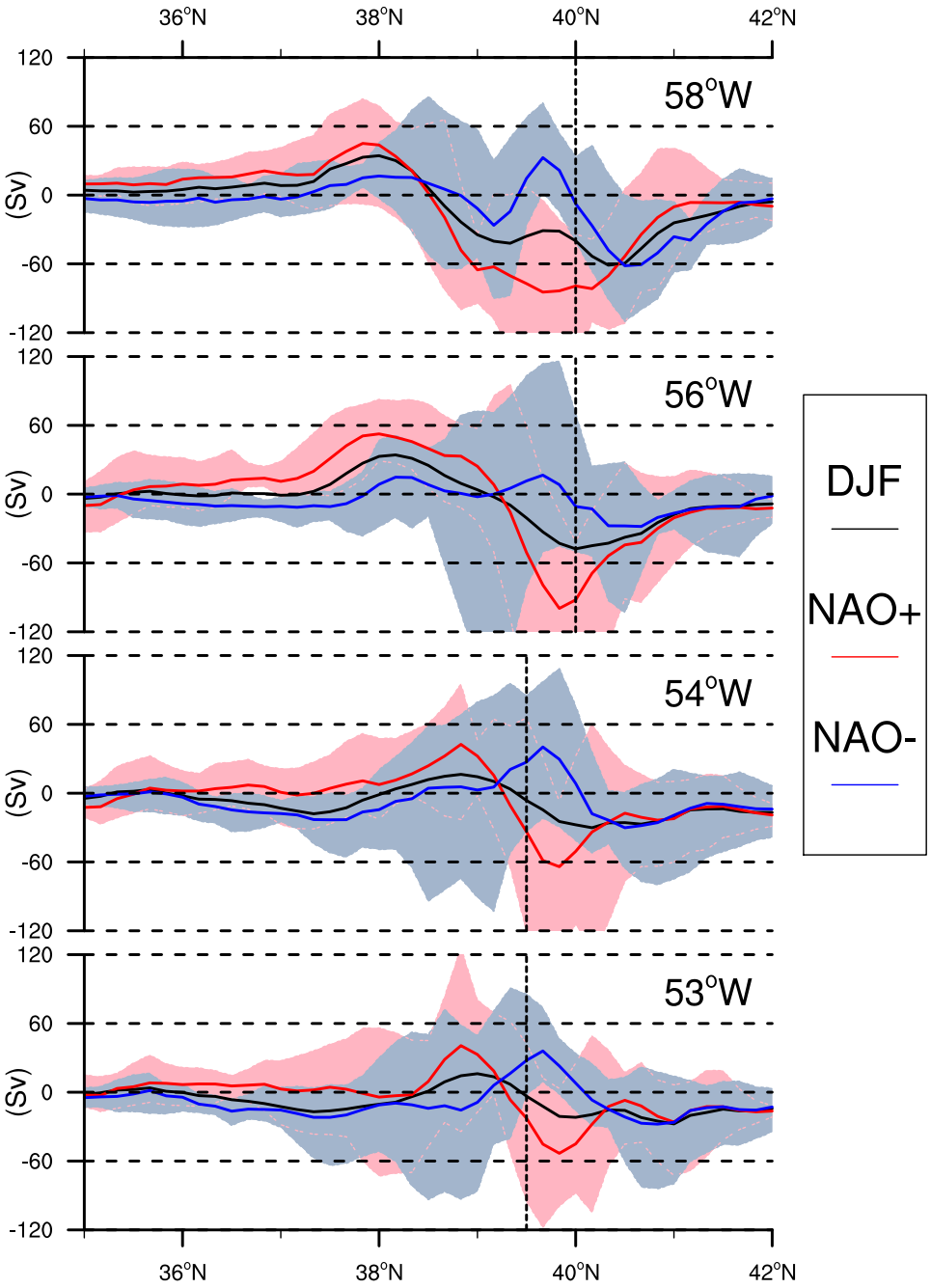

Figure 4.9: *Same as Figure 4.8 but for profiles downstream the NES.*

(southward) shift of the recirculation gyres at 70°W and a southward (northward) shift developing further downstream during positive (negative) NAO winters, both being significant as can be judged from the ensemble distributions. From velocity profiles, repeatedly measured by ship sections upstream of the NES over 4.5 years, *Rossby and Gottlieb* (1998) identified the dominant mode of interannual variability as indeed the location of the jet axis and not transport of the current. However, *Joyce et al.* (2000) found a positive correlation of their GS path index and the NAO, i.e., a northward path shift coincides with a positive NAO index. Since their index is based on an EOF analysis of the annual average position of the 15 °C isotherm in 200 m depth it includes the effect of the interannual variability on path shifts during all seasons. Therefore the effect of the NAO on the annual mean circulation was determined by binning the seasonal data into yearly intervals starting on the 1stof December. Finally these yearly chunks are assigned to the NAO states according to the NAO index of the winter they begin with and the average of each state is computed. The similarity of the DJF and annual averaged influences of the NAO (not shown) suggests that the response of the annual circulation is either rather uniform over the whole year or dominated by the DJF season. The apparent conflict with the results of *Joyce et al.* (2000) can be solved by putting the eddy driven circulation into context with the location of the mean jet axis. This suggests that during a positive phase the mean circulation is pushed northward and enhanced at 70°W and 66°W while it is decelerated at 68°W. During a negative phase, the transport is pushed to the south at 70°W and 68°W and decreased at 66°W.

Where the GS crosses the NES (at 62°W), the interannual variability is only very weak but there is still a significant increase of variability at the location of the mean current. Further downstream the character of variability changes from latitudinal shifts to a pronounced amplification of the DJF circulation pattern during positive NAO winters, shown in Figure 4.9. Both the cyclonic and anticyclonic recirculation gyres are located in a way to increase the mean transport and the interannual signal of the cyclonic recirculation cell is surprisingly significant for all shown sections. This is also true for the strength of the anticyclonic cell south of the mean current, however, only up to 56°W. But even far off the mean Stream path, at about 36°N to 37°N, there are significant differences between the ensemble distributions of the two NAO phases. Finally, the impact of the NAO on annual averaged streamfunction, introduced above, also suggest an increase of transport of the mean current since the mean current axis coincides with downward sloping streamfunction, although the amplitude is less pronounced than that of the DJF signal. These apparent and significant differences of ocean transport related to the changes of atmospheric circulation clearly supports the idea of an quasi-instantaneous and therefore local response of the EMF to the NAO.

Chapter 5

Discussion and Conclusion

The idea of EMF driving the recirculation gyres in the GSER is supported by the results presented in Section 4.1. The relative importance of this forcing to the other terms in the vorticity balance (3.13), i.e. mean flow advection and JEBAR, is still not answered at this point. Both mean flow advection (*Fofonoff*, 1954; *Marshall and Nurser*, 1986; *Greatbatch*, 1987) and JEBAR (*Holland*, 1973; *Mellor et al.*, 1982; *Greatbatch et al.*, 1991) have been proposed to explain the recirculation of the GS. Surface velocities derived from satellite altimeter data can be used to produce an estimate of the effect of mean flow advection. With identical assumptions about the vertical velocity profile, the SWM can be used to estimate the barotropic transport due to mean flow advection. The resulting streamfunction is shown in Figure 5.1. It exhibits strong recirculation cells at the vicinity of the mean currents path associated with bends of the stream. However, downstream of the NES these recirculation cells are not strongly connected and do not form a closed alongstream gyre. Upstream of the NES there is a recirculation cell on the warm flank of the current. Since the SWM is linear, both the EMF experiment and the mean flow advection experiment can be summed up and the result (also shown in Figure 5.1) does show some improvement on the EMF case when compared to the result of *Bryan et al.* (2007), especially upstream of the NES and downstream of the Mann eddy. This is an indication that in these regions the mean flow advection may be an important contribution to the vorticity balance (3.13) and can not be neglected. However, in the Reynolds-averaged form, variability is solely captured by the EMF due to the choice of a temporal invariant mean flow. Hence the results about variability incorporate the effect of velocity variability on all timescales, not only the effect of mesoscale eddies. It should be noted at this point that a clearer distinction between the effect of the two types of variability, i.e. mean flow and mesoscale eddies, could be made by defining the eddy velocity as the high frequency tail of the velocity spectrum and the mean flow as the residual. Assumptions about the cut-off frequency could be made from the

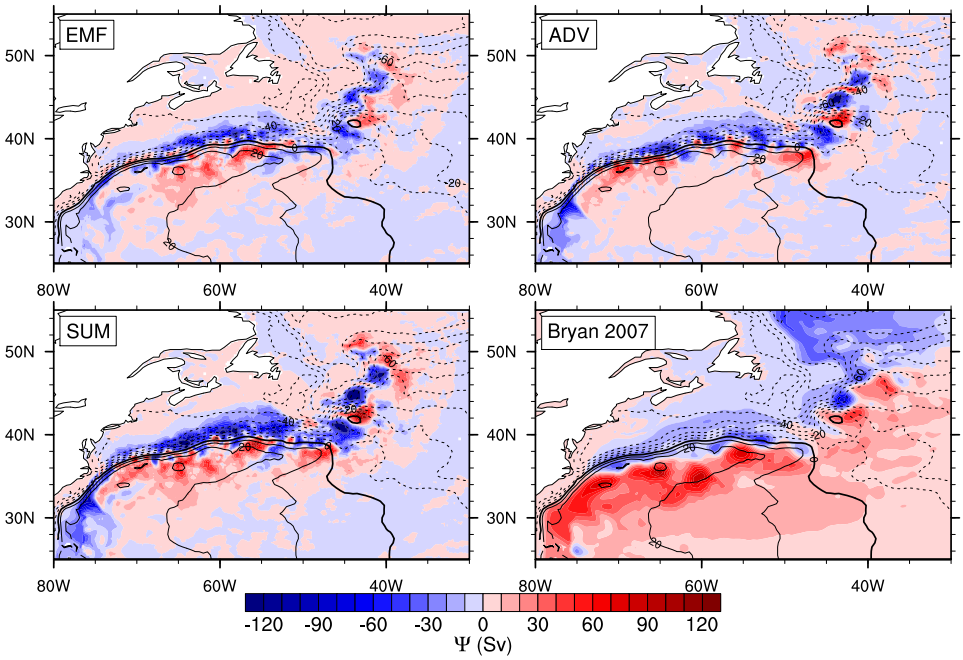

Figure 5.1: *Barotropic transport streamfunction* Ψ *in unit of Sverdrup associated with the (EMF) long-term mean Reynolds stress (same as Figure 4.1), (ADV) mean flow advection and (SUM) the sum of the latter two. (Bryan2007) is the same as Figure 4.3. Mean dynamic ocean topography (Niiler et al., 2003) is contoured in each plot with an interval of* 10 cm.

decorrelation timescale of the surface velocity. Another approach was made by *Penduff et al.* (2004) who computed EKE from the 12 month running variance of the velocity data to exclude interannual variability of the mean flow. However, since the time scales of seasonal fluctuation of the mean flow and mesoscale turbulent motion overlap a clear distinction of these two can not be achieved with any of the above mentioned methods.

In the vicinity of the separation point near Cape Hatteras and upstream of it the sum of both momentum flux contributions to the barotropic transport still disagree with both the mean dynamic ocean topography (*Niiler et al.*, 2003) and the results by *Bryan et al.* (2007). A possible explanation is the influence of the JEBAR term. *Greatbatch et al.* (1991) demonstrated that the JEBAR is capable of producing a anticyclonic recirculation cell at the warm flank of the GS offshore and upstream of the separation point. This suggests the importance of JEBAR in the vorticity balance near Cape Hatteras.

As a consequence of the westerly momentum fluxed into the jet by mesoscale eddies the mean jet core gets accelerated and tightened. Both increase barotropic instability associated with the horizontal shear of the background flow field and hence favour the conversion of mean kinetic en-

ergy to EKE. The GS separates the relatively cold and fresh slope water from the warm Sargasso Sea water (*Csanady and Hamilton*, 1988) and this temperature front is maintained by mean flow advection. The temperature flux associated with the eddies embodied by warm core rings on the cold flank of the GS and cold core rings on its warm flank act to decrease the sharpness of the temperature front. Therefore available potential energy will be released due to mixing and baroclinic instability will decrease with increasing eddy activity. In an average sense, the processes of production and degradation of unstable conditions should balance and this balance could control the sharpness of the thermal front which is of importance for climate modelling (*Minobe et al.*, 2008). Yet ocean components of modern climate models are not able to resolve mesoscale oceanic motion, hence these motions have to be parameterised, usually by assuming a eddy diffusivity. In the case of the GSER the eddy momentum diffusivity appears to be negative since momentum is fluxed towards the jet core. The actual strength of eddy momentum diffusivity seems to have a considerable amount of variation and hence is likely to depend on the state of climate. However, the eddy diffusivity of tracer quantities, like temperature or salinity, is clearly positive, thus momentum and tracer diffusivity have to be considered separately.

The results of the variability experiments bear difficulties due to the lack of observations with which to assess transport. This is especially true for the region downstream of the NES, of which the author is not aware of any publication concerning seasonal transport variability. Upstream of the NES the model lacks the seasonal variation due to JEBAR forcing even though this is a region where JEBAR is thought to be important (*Greatbatch et al.*, 1991; *Mellor et al.*, 1982).

The influence of the NAO on the NA circulation is often investigated in the context of wind stress anomalies causing an enhancement of the subpolar and subtropical gyre (*DiNezio et al.*, 2009; *Sturges and Hong*, 2001; *Marshall et al.*, 2001) with implications for EKE (*Brachet et al.*, 2004; *Penduff et al.*, 2004; *Volkov*, 2005). These gyre scale responses to wind forcing will have a time lag of the order of a year (*Brachet et al.*, 2004) or longer (*Volkov*, 2005; *Qiu and Chen*, 2010) since adjustments to changed forcing conditions will be propagated by baroclinic Rossby waves. At this point it is worth to mention that the data time period reflects a mostly positive NAO phase on decadal time scales. Due to the nonlinear nature of the problem the presented results may only prove valid during similar conditions and some important features like the spatial distribution of the EMF might change during more negative or neutral NAO states, similar to the decadal modulation of the Kuroshio Extension as reported by *Qiu and Chen* (2010). Clearly longer time series of surface velocity data with similar temporal and spatial resolution are required to shed light on this question. Due to the long time lag, gyre scale processes can not explain the modelled transport variability. More localised effects have to be responsible for this quasi-instantaneous response to changes

of the atmospheric conditions as reported by *Chaudhuri et al.* (2009). Three possible explanations are: (i) local Ekman pumping due to changes of wind stress curl, which can tilt the pycnocline and therefore influence the baroclinic instability, (ii) the change of mechanical damping due to surface wind fluctuations (*Duhaut and Straub*, 2006; *Zhai and Greatbatch*, 2007) and (iii) thermal interaction with the atmosphere leading to a damping of thermal anomalies associated with GS rings (*Zhai and Greatbatch*, 2006). The first of these possibilities will have an effect on the production of EKE and therefore the EMF, whereas the latter two affect the rate of dissipation of EKE, but to assess their relative importance is beyond the scope of this thesis and should be subject to further research.

List of Figures

List of Tables

Bibliography

Amante, C., and B. W. Eakins (2009), ETOPO1 1 Arc-minute global relief model: procedures, data sources and analysis, *NOAA Technical Memorandum NESDIS NGDC-24*, p. 19.

Barsugli, J. J., and D. S. Battisti (1998), The Basic Effects of Atmosphere–Ocean Thermal Coupling on Midlatitude Variability, *Journal of the Atmospheric Sciences*, *55*(4), 477–493, doi:10.1175/1520-0469(1998)055<0477:TBEOAO>2.0.CO;2.

Bjerknes, J. (1964), Atlantic air-sea interaction, *Advances in Geophysics*, *10*(1), 1–82.

Böning, C. W. (1986), On the influence of frictional parameterization in wind-driven ocean circulation models, *Dynamics of Atmospheres and Oceans*, *10*(1), 63–92, doi:10.1016/0377-0265(86)90010-2.

Brachet, S., P.-Y. Le Traon, and C. Le Provost (2004), Mesoscale variability from a high-resolution model and from altimeter data in the North Atlantic Ocean, *Journal of Geophysical Research*, *109*(C12025), 1–16, doi:10.1029/2004JC002360.

Bryan, F., M. Hecht, and R. Smith (2007), Resolution convergence and sensitivity studies with North Atlantic circulation models. Part I: The western boundary current system, *Ocean Modelling*, *16*(3-4), 141–159, doi:10.1016/j.ocemod.2006.08.005.

Cayan, D. R. (1992), Latent and Sensible Heat Flux Anomalies over the Northern Oceans: The Connection to Monthly Atmospheric Circulation, *Journal of Climate*, *5*(4), 354–369, doi:10.1175/1520-0442(1992)005<0354:LASHFA>2.0.CO;2.

Chassignet, E., and Z. Garraffo (2001), Viscosity parameterization and the Gulf Stream separation, *From Stirring to Mixing in a Stratified Ocean*, pp. 37–41.

Chaudhuri, A., J. Bisagni, and A. Gangopadhyay (2009), Shelf water entrainment by Gulf Stream warm-core rings between 75°W and 50°W dur-

ing 1978–1999, *Continental Shelf Research*, *29*(2), 393–406, doi:10.1016/j.csr.2008.10.001.

Cione, J. J., S. Raman, and L. J. Pietrafesa (1993), The effect of Gulf Stream-induced baroclinicity on US East Coast winter cyclones, *Monthly Weather Review*, *121*(2), 421–430.

Csanady, G. T., and P. Hamilton (1988), Circulation of slopewater, *Continental Shelf Research*, *8*(5-7), 565–624, doi:10.1016/0278-4343(88)90068-4.

de Coëtlogon, G., C. Frankignoul, M. Bentsen, C. Delon, H. Haak, S. Masina, and A. Pardaens (2006), Gulf Stream variability in five oceanic general circulation models, *Journal of Physical Oceanography*, *36*(11), 2119–2135, doi:10.1175/JPO2963.1.

Dickinson, R. E. (1969), Theory of Planetary Wave-Zonal Flow Interaction, *Journal of the Atmospheric Sciences*, *26*(1), 73–81, doi:10.1175/1520-0469(1969)026<0073:TOPWZF>2.0.CO;2.

DiNezio, P. N., L. J. Gramer, W. E. Johns, C. S. Meinen, and M. O. Baringer (2009), Observed Interannual Variability of the Florida Current: Wind Forcing and the North Atlantic Oscillation, *Journal of Physical Oceanography*, *39*(3), 721–736, doi:10.1175/2008JPO4001.1.

Ducet, N., and P.-Y. Le Traon (2001), A comparison of surface eddy kinetic energy and Reynolds stresses in the Gulf Stream and the Kuroshio Current systems from merged TOPEX/Poseidon and ERS-1/2 altimetric data, *Journal of Geophysical Research*, *106*(C8), 16,603–16,622, doi:10.1029/2000JC000205.

Duhaut, T. H. A., and D. N. Straub (2006), Wind Stress Dependence on Ocean Surface Velocity: Implications for Mechanical Energy Input to Ocean Circulation, *Journal of Physical Oceanography*, *36*(2), 202–211, doi:10.1175/JPO2842.1.

Eden, C., and R. J. Greatbatch (2003), A Damped Decadal Oscillation in the North Atlantic Climate System, *Journal of Climate*, *16*(24), 4043–4060, doi:10.1175/1520-0442(2003)016<4043:ADDOIT>2.0.CO;2.

Eden, C., and J. Willebrand (2001), Mechanism of Interannual to Decadal Variability of the North Atlantic Circulation, *Journal of Climate*, *14*(10), 2266–2280, doi:10.1175/1520-0442(2001)014<2266:MOITDV>2.0.CO;2.

Fofonoff, N. P. (1954), Steady flow in a frictionless homogeneous ocean, *Journal of Marine Research*, *13*(3), 254–262.

Frankignoul, C., G. de Coëtlogon, T. M. Joyce, and S. Dong (2001), Gulf Stream Variability and Ocean–Atmosphere Interactions, *Journal of Physical Oceanography*, *31*(12), 3516–3529, doi:10.1175/1520-0485(2002)031<3516:GSVAOA>2.0.CO;2.

Fu, L.-l., J. Vazquez, and M. E. Parke (1987), Seasonal Variability of the Gulf Stream From Satellite Altimetry, *Journal of Geophysical Research*, *92*(C1), 749–754, doi:10.1029/JC092iC01p00749.

Fuglister, F. C. (1963), Gulf stream '60, *Progress In Oceanography*, *1*(1246), 265–373, doi:10.1016/0079-6611(63)90007-7.

Fuglister, F. C., and L. V. Worthington (1951), Some Results of a Multiple Ship Survey of the Gulf Stream, *Tellus*, *3*(1), 1–14.

Greatbatch, R. J. (1987), A model for the inertial recirculation of a gyre, *Journal of Marine Research*, *45*(3), 601–634, doi:10.1357/002224087788326821.

Greatbatch, R. J., A. F. Fanning, A. D. Goulding, and S. Levitus (1991), A Diagnosis of Interpentadal Circulation Changes in the North Atlantic, *Journal of Geophysical Research*, *96*(C12), 22,009–22,023, doi:10.1029/91JC02423.

Greatbatch, R. J., X. Zhai, J.-D. Kohlmann, and L. Czeschel (2010a), Ocean eddy momentum fluxes at the latitudes of the Gulf Stream and the Kuroshio extensions as revealed by satellite data, *Ocean Dynamics*, *60*(3), 617–628, doi:10.1007/s10236-010-0282-6.

Greatbatch, R. J., X. Zhai, M. Claus, L. Czeschel, and W. Rath (2010b), Transport driven by eddy momentum fluxes in the Gulf Stream Extension region, *Geophysical Research Letters*, *37*(24), 1–6, doi:10.1029/2010GL045473.

Hansen, D. V. (1970), Gulf stream meanders between Cape Hatteras and the Grand Banks, *Deep Sea Research and Oceanographic Abstracts*, *17*(3), 495–511, doi:10.1016/0011-7471(70)90064-1.

Heaps, N. S. (1971), On the numerical solution of the three-dimensional hydrodynamical equations for tides and storm surges, *Mémoires de la Société Royale des Sciences de Liège.*, *2*, 143–180.

Hogg, N. G. (1992), On the transport of the gulf stream between cape hatteras and the grand banks, *Deep Sea Research Part A. Oceanographic Research Papers*, *39*(7-8), 1231–1246, doi:10.1016/0198-0149(92)90066-3.

Hogg, N. G., R. S. Pickart, R. M. Hendry, and W. J. Smethie (1986), The northern recirculation gyre of the gulf Stream, *Deep Sea Research*

Part A. Oceanographic Research Papers, *33*(9), 1139–1165, doi:10.1016/0198-0149(86)90017-8.

Holland, W. R. (1973), Baroclinic and topographic influences on the transport in western boundary currents, *Geophysical & Astrophysical Fluid Dynamics*, *4*(1), 187–210, doi:10.1080/03091927208236095.

Holland, W. R., and P. B. Rhines (1980), An Example of Eddy-Induced Ocean Circulation, *Journal of Physical Oceanography*, *10*(7), 1010–1031, doi:10.1175/1520-0485(1980)010<1010:AEOEIO>2.0.CO;2.

Hoskins, B. J., and K. I. Hodges (2002), New Perspectives on the Northern Hemisphere Winter Storm Tracks, *Journal of the Atmospheric Sciences*, *59*(6), 1041–1061, doi:10.1175/1520-0469(2002)059<1041:NPOTNH>2.0.CO;2.

Hughes, C. W., and E. R. Ash (2001), Eddy forcing of the mean flow in the Southern Ocean, *Journal of Geophysical Research*, *106*(C2), 2713–2722, doi:10.1029/2000JC900332.

Hughes, C. W., and B. A. de Cuevas (2001), Why Western Boundary Currents in Realistic Oceans are Inviscid: A Link between Form Stress and Bottom Pressure Torques, *Journal of Physical Oceanography*, *31*(10), 2871–2885, doi:10.1175/1520-0485(2001)031<2871:WWBCIR>2.0.CO;2.

Hurrell, J. W. (1995), Decadal trends in the north atlantic oscillation: regional temperatures and precipitation., *Science (New York, N.Y.)*, *269*(5224), 676–9, doi:10.1126/science.269.5224.676.

Iselin, C. O. (1936), A study of the circulation of the western North Atlantic, *Papers in Physical Oceanography and Meteorology*, *4*(4), 101.

Jeffreys, H. (1926), On the dynamics of geostrophic winds, *Quarterly Journal of the Royal Meteorological Society*, *52*(217), 85–102, doi:10.1002/qj.49705221708.

Johns, W. E., T. J. Shay, J. M. Bane, and D. R. Watts (1995), Gulf Stream structure, transport, and recirculation near 68°W, *Journal of Geophysical Research*, *100*(C1), 817–838, doi:10.1029/94JC02497.

Joyce, T. M., and R. Zhang (2010), On the Path of the Gulf Stream and the Atlantic Meridional Overturning Circulation, *Journal of Climate*, *23*(11), 3146–3154, doi:10.1175/2010JCLI3310.1.

Joyce, T. M., C. Deser, and M. A. Spall (2000), The Relation between Decadal Variability of Subtropical Mode Water and the North Atlantic Oscillation, *Journal of Climate*, *13*(14), 2550–2569, doi:10.1175/1520-0442(2000)013<2550:TRBDVO>2.0.CO;2.

Keffer, T. (1985), The Ventilation of the World's Oceans: Maps of the Potential Vorticity Field, *Journal of Physical Oceanography*, *15*(5), 509–523.

Kelly, K. A., and S. T. Gille (1990), Gulf Stream Surface Transport and Statistics at 69°W from the Geosat Altimeter, *Journal of Geophysical Research*, *95*(C3), 3149–3161, doi:10.1029/JC095iC03p03149.

Kuo, H.-L. (1951), Vorticity Transfer as Related to the Development of the General Circulation, *Journal of Meteorology*, *8*(5), 307–315, doi:10.1175/1520-0469(1951)008<0307:VTARTT>2.0.CO;2.

Lazier, J. R. N. (1994), Observations in the Northwest Corner of the North Atlantic Current, *Journal of Physical Oceanography*, *24*(7), 1449–1463, doi:10.1175/1520-0485(1994)024<1449:OITNCO>2.0.CO;2.

Le Traon, P.-Y., F. Nadal, and N. Ducet (1998), An Improved Mapping Method of Multisatellite Altimeter Data, *Journal of Atmospheric and Oceanic Technology*, *15*(2), 522–534, doi:10.1175/1520-0426(1998)015<0522:AIMMOM>2.0.CO;2.

Lee, T., and P. Cornillon (1995), Temporal variation of meandering intensity and domain-wide lateral oscillations of the Gulf Stream, *Journal of Geophysical Research*, *100*(C7), 13,603–13,613, doi:10.1029/95JC01219.

Lorenz, E. N. (1967), *The nature and theory of the general circulation of the atmosphere*, 161 pp., World Meteorological Organization, Geneva.

Mann, C. R. (1967), The termination of the Gulf Stream and the beginning of the North Atlantic Current, *Deep Sea Research and Oceanographic Abstracts*, *14*(3), 337–359, doi:10.1016/0011-7471(67)90077-0.

Marshall, J., and G. Nurser (1986), Steady, free circulation in a stratified quasi-geostrophic ocean, *Journal of Physical Oceanography*, *16*(11), 1799–1813.

Marshall, J., and A. R. Plumb (2008), *Atmosphere, Ocean, and Climate Dynamics: An Introductory Text*, 319 pp., Academic Press, Cleveland.

Marshall, J., H. Johnson, and J. Goodman (2001), A Study of the Interaction of the North Atlantic Oscillation with Ocean Circulation, *Journal of Climate*, *14*(7), 1399–1421, doi:10.1175/1520-0442(2001)014<1399:ASOTIO>2.0.CO;2.

Mellor, G. L., C. R. Mechoso, and E. Keto (1982), A diagnostic calculation of the general circulation of the atlantic ocean, *Deep Sea Research Part A. Oceanographic Research Papers*, *29*(10), 1171–1192, doi:10.1016/0198-0149(82)90088-7.

Mesinger, F., and A. Arakawa (1976), Numerical methods used in atmospheric models, volume 1, *Global Atmospheric Research Program World Meteorological Organization*, *1*(17), 1–65.

Minobe, S., A. Kuwano-Yoshida, N. Komori, S.-P. Xie, and R. J. Small (2008), Influence of the Gulf Stream on the troposphere., *Nature*, *452*(7184), 206–9, doi:10.1038/nature06690.

Niiler, P. P., N. A. Maximeko, and J. C. McWilliams (2003), Dynamically balanced absolute sea level of the global ocean derived from near-surface velocity observations, *Geophysical Research Letters*, *30*(22), 3–6, doi:10.1029/2003GL018628.

Peña Molino, B., and T. M. Joyce (2008), Variability in the Slope Water and its relation to the Gulf Stream path, *Geophysical Research Letters*, *35*(3), 1–5, doi:10.1029/2007GL032183.

Pedlosky, J. (1987), *Geophysical fluid dynamics*, 710 pp., Springer, New York. US.

Penduff, T., B. Barnier, W. K. Dewar, and J. J. O'Brien (2004), Dynamical Response of the Oceanic Eddy Field to the North Atlantic Oscillation: A Model–Data Comparison, *Journal of Physical Oceanography*, *34*(12), 2615–2629, doi:10.1175/JPO2618.1.

Qiu, B., and S. Chen (2010), Eddy-mean flow interaction in the decadally modulating Kuroshio Extension system, *Deep Sea Research Part II: Topical Studies in Oceanography*, *57*(13-14), 1098–1110, doi:10.1016/j.dsr2.2008.11.036.

Rhines, P. B. (1969), Slow oscillations in an ocean of varying depth Part 2. Islands and seamounts, *Journal of Fluid Mechanics*, *37*(01), 191–205, doi:10.1017/S0022112069000486.

Richardson, P. L. (1985), Average velocity and transport of the Gulf Stream near 55W, *Journal of Marine Research*, *43*(1), 83–111, doi:10.1357/002224085788437343.

Rossby, T., and E. Gottlieb (1998), The Oleander Project: Monitoring the Variability of the Gulf Stream and Adjacent Waters between New Jersey and Bermuda, *Bulletin of the American Meteorological Society*, *79*(1), 5–18, doi:10.1175/1520-0477(1998)079<0005:TOPMTV>2.0.CO;2.

Rossby, T., C. Flagg, and K. Donohue (2010), On the variability of Gulf Stream transport from seasonal to decadal timescales, *Journal of Marine Research*, *68*(3), 503–522, doi:10.1357/002224010794657128.

Saravanan, R., and J. C. McWilliams (1998), Advective Ocean–Atmosphere Interaction: An Analytical Stochastic Model with Implications for Decadal Variability, *Journal of Climate*, *11*(2), 165–188, doi:10.1175/1520-0442(1998)011<0165:AOAIAA>2.0.CO;2.

Sato, O., and T. Rossby (1995), Seasonal and low frequency variations in dynamic height anomaly and transport of the Gulf Stream, *Deep Sea Research Part I: Oceanographic Research Papers*, *42*(1), 149–164, doi:10.1016/0967-0637(94)00034-P.

Schmitz, W. J. (1980), Weakly Depth-Dependent Segments of the North-Atlantic Circulation, *Journal of Marine Research*, *38*(1), 111–133.

Schmitz, W. J. J., and P. L. Richardson (1991), On the sources of the Florida Current, *Deep-sea research. Part A. Oceanographic research papers*, *38*(1), 379–409.

Scott, R. B., B. K. Arbic, C. L. Holland, A. Sen, and B. Qiu (2008), Zonal versus meridional velocity variance in satellite observations and realistic and idealized ocean circulation models, *Ocean Modelling*, *23*(3-4), 102–112, doi:10.1016/j.ocemod.2008.04.009.

Seager, R., D. S. Battisti, J. Yin, N. Gordon, N. Naik, A. C. Clement, and M. A. Cane (2002), Is the Gulf Stream responsible for Europe's mild winters?, *Quarterly Journal of the Royal Meteorological Society*, *128*(586), 2563–2586, doi:10.1256/qj.01.128.

Smith, R. D., M. E. Maltrud, F. O. Bryan, and M. W. Hecht (2000), Numerical Simulation of the North Atlantic Ocean at 1 / 10 °, *Journal of Physical Oceanography*, *30*(7), 1532–1561, doi:10.1175/1520-0485(2000)030<1532:NSOTNA>2.0.CO;2.

Stammer, D., and C. Wunsch (1999), Temporal changes in eddy energy of the oceans, *Deep Sea Research Part II: Topical Studies in Oceanography*, *46*(1-2), 77–108, doi:10.1016/S0967-0645(98)00106-4.

Starr, V. P. (1948), An essay on the general circulation of the earth's atmosphere, *Journal of Meteorology*, *5*, 39–43.

Stommel, H. M. (1948), The westward intensification of wind-driven ocean currents, *Trans. Amer. Geophys. Union*, *29*(2), 202–206.

Sturges, W., and B. G. Hong (2001), Gulf Stream Transport Variability at Periods of Decades, *Journal of Physical Oceanography*, *31*(5), 1304–1312, doi:10.1175/1520-0485(2001)031<1304:GSTVAP>2.0.CO;2.

Thompson, R. O. R. Y. (1971), Why There is an Intense Eastward Current in the North Atlantic but not in the South Atlantic, *Journal of Physical Oceanography*, *1*(3), 235–237, doi:10.1175/1520-0485(1971)001<0235:WTIAIE>2.0.CO;2.

Tracey, K. L., and D. R. Watts (1986), On Gulf Stream Meander Characteristics Near Cape Hatteras, *Journal of Geophysical Research*, *91*(C6), 7587–7602, doi:10.1029/JC091iC06p07587.

Trenberth, K. E., and J. M. Caron (2001), Estimates of Meridional Atmosphere and Ocean Heat Transports, *Journal of Climate*, *14*(16), 3433–3443, doi:10.1175/1520-0442(2001)014<3433:EOMAAO>2.0.CO;2.

Veronis, G. (1966), Wind-driven ocean circulation–Part 2. Numerical solutions of the non-linear problem, *Deep Sea Research*, *13*(1), 31–55.

Volkov, D. L. (2005), Interannual Variability of the Altimetry-Derived Eddy Field and Surface Circulation in the Extratropical North Atlantic Ocean in 1993–2001, *Journal of Physical Oceanography*, *35*(4), 405–426, doi:10.1175/JPO2683.1.

Wardle, R., and J. Marshall (2000), Representation of Eddies in Primitive Equation Models by a PV Flux, *Journal of Physical Oceanography*, *30*(10), 2481–2503, doi:10.1175/1520-0485(2000)030<2481:ROEIPE>2.0.CO;2.

Webster, F. (1961), The Effect of Meanders on the Kinetic Energy Balance of the Gulf Stream, *Tellus*, *13*(3), 392–401, doi:10.1111/j.2153-3490.1961.tb00100.x.

Worthington, L. V. (1954), Three Detailed Cross-Sections of the Gulf Stream., *Tellus*, *6*(2), 116–123, doi:10.1111/j.2153-3490.1954.tb01101.x.

Worthington, L. V. (1976), *On the North Atlantic Circulation*, 110 pp., Johns Hopkins University Press.

Wunsch, C. (1997), The Vertical Partition of Oceanic Horizontal Kinetic Energy, *Journal of Physical Oceanography*, *27*(8), 1770–1794, doi:10.1175/1520-0485(1997)027<1770:TVPOOH>2.0.CO;2.

Wunsch, C. (2005), The Total Meridional Heat Flux and Its Oceanic and Atmospheric Partition, *Journal of Climate*, *18*(21), 4374–4380, doi:10.1175/JCLI3539.1.

Wüst, G. (1935), Die Stratosphäre des Atlantischen Ozeans, *Wiss. Erg. d. DAE 'Meteor'1925–1927*, *6*(2), 1—-288.

Yu, L., and R. A. Weller (2007), Objectively Analyzed Air–Sea Heat Fluxes for the Global Ice-Free Oceans (1981–2005), *Bulletin of the American Meteorological Society*, *88*(4), 527–539, doi:10.1175/BAMS-88-4-527.

Zhai, X., and R. J. Greatbatch (2006), Surface eddy diffusivity for heat in a model of the northwest Atlantic Ocean, *Geophysical Research Letters*, *33*(24), 1–5, doi:10.1029/2006GL028712.

Zhai, X., and R. J. Greatbatch (2007), Wind work in a model of the northwest Atlantic Ocean, *Geophysical Research Letters*, *34*(4), 1–4, doi: 10.1029/2006GL028907.

Zhai, X., R. J. Greatbatch, and J. Sheng (2004), Diagnosing the role of eddies in driving the circulation of the northwest Atlantic Ocean, *Geophysical Research Letters*, *31*(23), 2–5, doi:10.1029/2004GL021146.

Zhai, X., R. J. Greatbatch, and J.-D. Kohlmann (2008), On the seasonal variability of eddy kinetic energy in the Gulf Stream region, *Geophysical Research Letters*, *35*(24), 1–6, doi:10.1029/2008GL036412.

Zhang, R., and G. K. Vallis (2007), The Role of Bottom Vortex Stretching on the Path of the North Atlantic Western Boundary Current and on the Northern Recirculation Gyre, *Journal of Physical Oceanography*, *37*(8), 2053–2080, doi:10.1175/JPO3102.1.

Declaration by Candidate

I hereby declare that this thesis is my own work and effort and that it has not been submitted anywhere for any award. Where other sources of information have been used, they have been acknowledged.

Kiel, October 11, 2011

(Martin Claus)